Supplement of Earth Syst. Sci. Data, 17, 6445–6460, 2025
https://doi.org/10.5194/essd-17-6445-2025-supplement

Supplement of

Multi-spatial scale assessment and multi-dataset fusion of global terrestrial evapotranspiration datasets

Yi Wu et al.

Correspondence to: Chiyuan Miao (miaocy@bnu.edu.cn)

Text S1. Flux sites and data preprocessing

The ET from FLUXNET has been quality controlled and pre-processed to improve cross-site consistency and comparability using the harmonised methodology described in Pastorello et al. (2020). Meteorological data were filled by two independent methods: marginal distribution sampling (variables with _F_MDS suffix) and ERA-Interim (variables with _F_ERA suffix). The final missing-fill product (variables with _F suffix) consists of direct measurements and missing-fill records. In this study, latent heat fluxes were filled using half-hourly (hourly) precipitation (P_F in mm) and MDS methods (LE_F_MDS in $W{\cdot}m^{-2}$). Record lengths for each site ranged from 1 to 24 years. For latent heat fluxes, the data processing steps (screening criteria) were as follows: (1) First, only data with a continuous coverage of at least 3 years were collected. (2) Data with negative latent heat fluxes were excluded. (3) Because flux data from nighttime eddy covariance measurements are missing and have large errors (Mahrt, 1999; Yuan et al., 2021), the study extracted only daytime latent heat flux data. Daytime is defined as 7:00 to 19:00 local time (McGloin et al., 2019; Yuan et al., 2021). The study did not use incident shortwave radiation to define daytime, as nighttime occasionally has larger values. (4) To avoid high likelihood of dew evaporation (Knauer et al., 2018), the study excluded data with relative humidity above 95%, as it can strongly affect evapotranspiration measurements. (5) To avoid intercepted evaporation and sensor saturation at high relative humidity (Medlyn et al., 2017), data during and up to 6 hours after rainfall were excluded. (6) To reduce the impact of outliers on half-hourly-scale data, data below the 5% percentile and above the 95% percentile in latent heat flux were excluded. Half-hourly evapotranspiration (in mm) was obtained from the latent heat flux calculations. For precipitation, only (2) and (6) were considered in the data processing steps. Half-hourly data (precipitation and evapotranspiration) were finally computed on a monthly scale. In the end, 174 stations were retained.

Text S2. Verification of energy balance closure

There are many computational methods for evaluating and analysing energy balance closure, and in order to be able to comprehensively evaluate the state of energy balance closure at each flux site, this study used the least-squares linear regression (ordinary least squares [OLS]) and the energy balance ratio (EBR) methods. The study adjusted some of the flux data to ensure the quality of the data used in this study. Site energy closure is a key indicator of flux data quality (Zhu et al., 2016).

$$Res = R_n - H - \lambda E - G \tag{S1}$$

where R_n is the net radiation (W·m^{-2}), H is the sensible heat flux (W·m^{-2}), λE is the latent heat flux (W·m^{-2}), and G is the soil heat flux (W·m^{-2}). The difference between net radiation and soil heat flux is the available energy. In most cases, the available energy is greater than the sum of sensible and latent heat. In general, the surface energy balance closure (the sum of sensible and latent heat fluxes divided by the available energy) is usually in the range of 70% to 90% (Foken et al., 2006).

Text S3. Water balance method

At the basin scale, changes in precipitation, runoff, ET, and total water storage constitute the watershed water balance, and the variables in the water balance can be obtained relatively accurately except for ET; therefore, watershed ET is usually calculated using the water balance method, and the method is often used as a standard method for watershed ET estimation (Xu et al., 2019). Based on the water balance principle, the actual evapotranspiration is calculated using the following equation

$$ET = P - R - TWSC \tag{S2}$$

where P represents total precipitation in the basin, R represents total runoff in the basin, and $TWSC$ represents the change in total water storage. Basin ET values obtained based on water balance are often used as reference values to verify the accuracy of ET datasets at the basin scale (Senay et al., 2011; Zhang et al., 2010). Equation 2 can be used to assess various global ET datasets in a basin but is not applicable to the basins where R is not available. TWSC should be considered when data span less than 10 years, especially for monthly-scale ET assessments. The formula for the region is as follows:

$$TWSC(i) = \frac{TWSA(i+1) - TWSA(i-1)}{2\Delta i} \tag{S3}$$

Here, $TWSA$ is the total water storage anomaly, which can be obtained from GRACE data(Tapley et al., 2019). When the data spans more than 10 years, it can be ignored. Thus, the above equation can be written as $ET = P - R$.

Text S4. Three-cornered hat (TCH) method

The study uses the three-cornered hat (TCH) method to calculate the errors and uncertainties of thirty evapotranspiration datasets without any prior knowledge.

The details of the TCH method are described below. Assuming that there are n different evapotranspiration datasets $\{ET_i\}_{i=1,2,\ldots,N}$, i, then the i^{th} ET dataset ET_i can generally be expressed as

$$ET_i = ET_{true} + \varepsilon_i, i = 1,2,\ldots,n \tag{S4}$$

Among them, ET_{true} is the true surface ET, and ε_i is the observation error of ET_i. Since the real ET value cannot be obtained, any ET dataset is selected as the reference value, and the difference sequence between the remaining ET datasets and the reference value is obtained as

$$y_i = ET_i - ET_{ref} = \varepsilon_i - \varepsilon_{ref}, i = 1,2,\ldots,n-1 \tag{S5}$$

ET_{ref} is an arbitrarily selected reference ET dataset. The error analysis results of the TCH method do not depend on the selection of the reference dataset (Ferreira et al., 2016). The covariance matrix of Y can be represented by $S = cov(Y)$. Introducing the unknown noise covariance matrix R (R is a symmetric matrix), then its relationship with S is

$$S = J \cdot R \cdot J^T \tag{S6}$$

where J is represented as

$$J_{n-1,n} = \begin{bmatrix} 1 & 1 & \cdots & 0 & -1 \\ 0 & 0 & \cdots & 0 & -1 \\ \vdots & \vdots & \ddots & \vdots & \vdots \\ 0 & 0 & 0 & \cdots & -1 \end{bmatrix} \tag{S7}$$

Matrix R is defined as

$$R = \begin{bmatrix} \sigma_{11} & \sigma_{12} & \cdots & \sigma_{1n} \\ \sigma_{12} & \sigma_{22} & \cdots & \sigma_{21} \\ \vdots & \vdots & \ddots & \vdots \\ \sigma_{1n} & \sigma_{21} & \cdots & \sigma_{nn} \end{bmatrix} \tag{S8}$$

Among these, $\sigma_{ii} = cov(\varepsilon_i, \varepsilon_j)$, $(i, j = 1, 2, \cdots, n)$, is the covariance of time series ε_i and ε_j. However, Eq. (8) cannot be solved as the number of unknown elements is larger than the number of equations. Therefore, the remaining parameters require a reasonable approach to obtain a unique value. Galindo and Palacio (1999) proposed a method based on Kuhn-Tucker theory, and the objective function is given below:

$$F_{(\sigma_{1n},\ldots,\sigma_{nn})} = \frac{1}{K^2}\sum_{i<j}^{n}(\sigma_{ij})^2 \tag{S9}$$

Here, $K = \sqrt[N-1]{\det(S)}$. The constraint H is

$$H_{(\sigma_{1n},\ldots,\sigma_{nn})} = -\frac{|Q|}{|S|\cdot K} < 0 \tag{S10}$$

Q is a diagonal matrix, and the elements on its diagonal are $\sigma_{11}, \sigma_{22}, \ldots, \sigma_{nn}$. The square root of the Q diagonal values are considered to be the uncertainty of evaluated ET. The ratio of the uncertainty to the time series mean value is the relative uncertainty.

Text S5. Taylor diagram

The Taylor diagram was first proposed by Taylor and is mainly used to evaluate the ability of different models to simulate a variable. The plot combines three evaluation metrics: the correlation coefficient, the root mean square error, and the ratio of the standard deviations of the simulated and observed fields on a single polar plot. See Taylor for specific formulas. Standardized Taylor diagram normalize the standard deviation and root mean square error to eliminate their physical units of measure. When the correlation coefficient is larger, the root-mean-square error is smaller, and the ratio of the standard deviation of the simulated values to that of the observed values tends to be closer to 1, it indicates that the simulation results are in good agreement with the measured data, i.e., the model simulation results are highly reliable. In this study, a standardized Taylor diagram was used for the comprehensive assessment of the global ET dataset.

Text S6. Bayesian model average (BMA) fusion scheme

Bayesian model averaging (BMA) has recently been proposed as a statistical method to calibrate forecast ensembles from numerical weather models. Successful implementation of BMA, however, requires accurate estimates of the weights and variances of the individual competing models in the ensemble. In this study, we use the DiffeRential Evolution Adaptive Metropolis (DREAM) Markov Chain Monte Carlo (MCMC) algorithm for estimating the BMA weights and variances (Vrugt et al., 2008). The formulas are described in detail in Vrugt et al. (2008).

Text S7. Weighting scheme for ET dataset fusion

Analysis was performed based on the grid scale of each ET dataset. Among these datasets, 1982–2011 are the common coverage years for all ET datasets, and their weights are calculated as detailed in section 2.2 of the main text. As for the years with non-overlapping coverage 1980–1981 and 2012–2020, the weights for each year are obtained by filtering all ET datasets covering that year for BMA analyses to obtain the corresponding weights (see Fig. S5). For example, there are a total of 27 ET datasets covering the year 1980, and the weights obtained from the BMA analysis based on these 27 ET datasets are used as the weights of these 27 datasets in 1980; there are a total of 19 ET datasets covering the year 2019, and the weights obtained from the BMA analysis based on these 19 ET datasets are used as the weights of these 19 datasets in 2019.

Text S8. Bayesian-Three Cornered Hat (BTCH)

The BTCH method is utilized to generate an accurate ET product by combining various ET datasets (Tavella and Premoli, 1994). The probability density function (PDF) for the ith ET product (ET_i) can be expressed as,

$$p(ET_i|ET_t) = \frac{1}{\sigma_i\sqrt{2\pi}}\exp\left[-\frac{\varepsilon_i^2}{2\sigma_i^2}\right] = L(ET_t|ET_i)(\varepsilon_i = ET_i - ET_t) \qquad \text{(S11)}$$

where ET_t is the true value of ET. ε_i and σ_i are a zero-mean white noise and error variance of the ith ET product, respectively. $L(\cdot)$ is the likelihood function.

Similarly, the PDF for jth ET product (ET_j) can be expressed as,

$$p\left(ET_j|ET_t\right) = \frac{1}{\sigma_j\sqrt{2\pi}}\exp\left[-\frac{\varepsilon_j^2}{2\sigma_j^2}\right] = L\left(ET_t|ET_j\right)\left(\varepsilon_j = ET_j - ET_t\right) \qquad \text{(S12)}$$

where ε_j and σ_j are a zero-mean white noise and error variance of the jth ET product. The maximum likelihood of true ET (ET_t) is the maximum value of its joint probability distribution,

$$\max L\left(ET_t|ET_i, ET_j\right) = p(ET_i|ET_t)\, p\left(ET_j|ET_t\right) = \frac{1}{2\pi\sigma_i\sigma_j}\exp\left[-\frac{\varepsilon_i^2}{2\sigma_i^2} - \frac{\varepsilon_j^2}{2\sigma_j^2}\right] \text{(S13)}$$

In order to obtain the maximum likelihood value of ET_t in Equation (S13), the cost function J is defined as,

$$J(ET_t) = \frac{\varepsilon_i^2}{2\sigma_i^2} + \frac{\varepsilon_j^2}{2\sigma_j^2} = \frac{1}{2}\left[\frac{(ET_i - ET_t)^2}{\sigma_i^2} + \frac{\left(ET_j - ET_t\right)^2}{\sigma_j^2}\right] \qquad \text{(S14)}$$

By setting the first variation of $J(ET_t)$ to zero (i.e., $\delta J(ET_t) = 0$), ET_t can be obtained as,

$$ET_t = \frac{\sigma_i^2}{\sigma_i^2 + \sigma_j^2} ET_i + \frac{\sigma_j^2}{\sigma_i^2 + \sigma_j^2} ET_j \tag{S15}$$

If we define $ET_t = \omega_i ET_i + \omega_j ET_j$, then

$$\omega_i = \frac{\sigma_i^2}{\sigma_i^2 + \sigma_j^2}, \omega_j = \frac{\sigma_j^2}{\sigma_i^2 + \sigma_j^2} \tag{S16}$$

Similar to Equation (S15), ET_t can be obtained via $ET_t = \omega_1 ET_1 + \cdots + \omega_N ET_N$ when there are N sets of ET products. The weight of each ET product (e.g., ω_k) can be obtained by minimizing a similar cost function (Equation (S14)) as,

$$\omega_k = \frac{\prod_{i=1, i \neq k}^{N} \sigma_i^2}{\sum_{k=1}^{N} (\prod_{i=1, i \neq k}^{N} \sigma_i^2)} \tag{S17}$$

The error covariance (σ_i) of each ET product can be obtained using the three-cornered hat (TCH) method.

Since ET_t is not available, the difference between $(N-1)$ ET products and a reference ET product (ET_R) (chosen arbitrarily from N ET products) can be expressed as,

$$Y_{i,M} = ET_i - ET_R = \varepsilon_i - \varepsilon_R, i = 1,2,\cdots,N-1 \tag{S18}$$

where Y is the difference matrix with $(N-1)$ rows and M columns (M is the total number of time samples in each ET product). The covariance matrix (**S**) of **Y** is defined as (Galindo and Palacio, 2003),

$$\mathbf{S} = cov(\mathbf{Y}) \tag{S19}$$

where $cov(\cdot)$ is the covariance operator. The unknown covariance matrix of the individual noise **R** is related to **S** via,

$$\mathbf{S} = \mathbf{J} \cdot \mathbf{R} \cdot \mathbf{J}^{\boldsymbol{T}} \tag{S20}$$

where **J** is the identity matrix, and can be defined as,

$$\mathbf{J}_{N-1,N} = \begin{bmatrix} 1 & 0 & \cdots & 0 & -1 \\ 0 & 1 & \cdots & 0 & -1 \\ \vdots & \vdots & \vdots & \vdots & \vdots \\ 0 & 0 & 0 & \cdots & -1 \end{bmatrix} \tag{S21}$$

and matrix $\mathbf{R}$ is defined as,

$$\mathbf{R}=\begin{bmatrix}\sigma_{11} & \sigma_{12} & \cdots & \sigma_{1N}\\ \sigma_{12} & \sigma_{22} & \cdots & \sigma_{2N}\\ \vdots & \vdots & \vdots & \vdots\\ \sigma_{1N} & \sigma_{2N} & \cdots & \sigma_{NN}\end{bmatrix} \tag{S22}$$

where $\sigma_{ij}=cov(\varepsilon_i-\varepsilon_j)$. There are $N\times(N+1)/2$ unknowns in Equation (S20) (number of distinct elements of $\mathbf{R}$), but there are only $N\times(N-1)/2$ equations (number of distinct elements of $\mathbf{S}$). Thus, there remain N free parameters that must be reasonably determined to obtain a unique solution (Galindo and Palacio, 2003). To determine the N free parameters, the following objective function is minimized based on the Kuhn–Tucker theorem.

The Kuhn–Tucker theorem is proposed by Galindo and Palacio (1999), and the objective function is defined as,

$$F_{(\sigma_{1N},\cdots,\sigma_{NN})}=\frac{1}{\mathbf{K}^2}\cdot\sum_{i<j}^{N}\left(\sigma_{ij}\right)^2 \tag{S23}$$

where $\mathbf{K}=\sqrt[N-1]{\det(\mathbf{S})}$. The constraint function is given by,

$$H_{(\sigma_{1N},\cdots,\sigma_{NN})}=-\frac{|\mathbf{Q}|}{|\mathbf{S}|\cdot\mathbf{K}}<0 \tag{S24}$$

where $\mathbf{Q}$ is a diagonal matrix with elements $\sigma_{11},\cdots,\sigma_{NN}$ on its diagonal. These arrays can be calculated by minimizing Equation (S23) through the initial condition iterations. The square root of the diagonal elements of $\mathbf{R}$ (i.e., $\sigma_{11},\sigma_{22},\cdots,\sigma_{NN}$) represent the relative uncertainty of each ET product (Xu et al., 2019). The readers are referred to Xu et al. (2019) for detailed information on the TCH approach.

The ensemble mean (EM) method is used to also integrate the ten long-term gridded ET products and generate an ET product. This method just simply calculates the average of ET products as follows:

$$ET_{EM}=\frac{1}{N}\cdot\sum_{i=1}^{N}ET_i \tag{S25}$$

References

Ferreira, V. G., Montecino, H. D. C., Yakubu, C. I., and Heck, B.: Uncertainties of the Gravity Recovery and Climate Experiment time-variable gravity-field solutions based on three-cornered hat method, JARS, 10, 015015, https://doi.org/10.1117/1.JRS.10.015015, 2016.

Foken, T., Wimmer, F., Mauder, M., Thomas, C., and Liebethal, C.: Some aspects of the energy balance closure problem, Atmospheric Chemistry and Physics, 6, 4395–4402, https://doi.org/10.5194/acp-6-4395-2006, 2006.

Galindo, F. J. and Palacio, J.: Estimating the Instabilities of N Correlated Clocks, in: Proceedings of the 31th Annual Precise Time and Time Interval Systems and Applications Meeting, Proceedings of the 31th Annual Precise Time and Time Interval Systems and Applications Meeting, 285–296, 1999.

Galindo, F. J. and Palacio, J.: Post-processing ROA data clocks for optimal stability in the ensemble timescale, Metrologia, 40, S237, https://doi.org/10.1088/0026-1394/40/3/301, 2003.

Knauer, J., Zaehle, S., Medlyn, B. E., Reichstein, M., Williams, C. A., Migliavacca, M., De Kauwe, M. G., Werner, C., Keitel, C., Kolari, P., Limousin, J.-M., and Linderson, M.-L.: Towards physiologically meaningful water-use efficiency estimates from eddy covariance data, Global Change Biology, 24, 694–710, https://doi.org/10.1111/gcb.13893, 2018.

Mahrt, L.: Stratified Atmospheric Boundary Layers, Boundary-Layer Meteorology, 90, 375–396, https://doi.org/10.1023/A:1001765727956, 1999.

McGloin, R., Šigut, L., Fischer, M., Foltýnová, L., Chawla, S., Trnka, M., Pavelka, M., and Marek, M. V.: Available Energy Partitioning During Drought at Two Norway Spruce Forests and a European Beech Forest in Central Europe, Journal of Geophysical Research: Atmospheres, 124, 3726–3742, https://doi.org/10.1029/2018JD029490, 2019.

Medlyn, B. E., De Kauwe, M. G., Lin, Y.-S., Knauer, J., Duursma, R. A., Williams, C. A., Arneth, A., Clement, R., Isaac, P., Limousin, J.-M., Linderson, M.-L., Meir, P., Martin-StPaul, N., and Wingate, L.: How do leaf and ecosystem measures of water-use efficiency compare?, New Phytologist, 216, 758–770, https://doi.org/10.1111/nph.14626, 2017.

Pastorello, G., Trotta, C., Canfora, E., Chu, H., Christianson, D., Cheah, Y.-W., Poindexter, C., Chen, J., Elbashandy, A., Humphrey, M., Isaac, P., Polidori, D., Reichstein, M., Ribeca, A., van Ingen, C., Vuichard, N., Zhang, L., Amiro, B., Ammann, C., Arain, M. A., Ardö, J., Arkebauer, T., Arndt, S. K., Arriga, N., Aubinet, M., Aurela, M., Baldocchi, D., Barr, A., Beamesderfer, E., Marchesini, L. B., Bergeron, O., Beringer, J., Bernhofer, C., Berveiller, D., Billesbach, D., Black, T. A., Blanken, P. D., Bohrer, G., Boike, J., Bolstad, P. V., Bonal, D., Bonnefond, J.-M., Bowling, D. R., Bracho, R., Brodeur, J., Brümmer, C., Buchmann, N., Burban, B., Burns, S. P., Buysse, P., Cale, P., Cavagna, M., Cellier, P., Chen, S., Chini, I., Christensen, T. R., Cleverly, J., Collalti, A., Consalvo, C., Cook, B. D., Cook, D., Coursolle, C., Cremonese, E., Curtis, P. S., D'Andrea, E., da Rocha, H., Dai, X., Davis, K. J., Cinti, B. D., Grandcourt, A. de, Ligne, A. D., De Oliveira, R. C., Delpierre, N., Desai, A. R., Di Bella, C. M., Tommasi, P. di, Dolman, H., Domingo, F., Dong, G., Dore, S., Duce, P., Dufrêne, E., Dunn, A., Dušek, J., Eamus, D., Eichelmann, U., ElKhidir, H. A. M., Eugster, W., Ewenz, C. M., Ewers, B., Famulari, D., Fares, S., Feigenwinter, I., Feitz, A., Fensholt, R., Filippa, G., Fischer, M., Frank, J., Galvagno, M., et al.: The FLUXNET2015 dataset and the ONEFlux processing pipeline for eddy covariance data, Sci Data, 7, 225, https://doi.org/10.1038/s41597-020-0534-3, 2020.

Senay, G. B., Leake, S., Nagler, P. L., Artan, G., Dickinson, J., Cordova, J. T., and Glenn, E. P.: Estimating basin scale evapotranspiration (ET) by water balance and remote sensing methods, Hydrological Processes, 25, 4037–4049, https://doi.org/10.1002/hyp.8379, 2011.

Tapley, B. D., Watkins, M. M., Flechtner, F., Reigber, C., Bettadpur, S., Rodell, M., Sasgen, I., Famiglietti, J. S., Landerer, F. W., Chambers, D. P., Reager, J. T., Gardner, A. S., Save, H., Ivins, E. R., Swenson, S. C., Boening, C., Dahle, C., Wiese, D. N., Dobslaw, H., Tamisiea, M. E., and Velicogna, I.: Contributions of GRACE to understanding climate change, Nat. Clim. Chang., 9, 358–369, https://doi.org/10.1038/s41558-019-0456-2, 2019.

Tavella, P. and Premoli, A.: Estimating the Instabilities of N Clocks by Measuring Differences of their Readings, Metrologia, 30, 479, https://doi.org/10.1088/0026-1394/30/5/003, 1994.

Vrugt, J. A., Diks, C. G. H., and Clark, M. P.: Ensemble Bayesian model averaging using Markov Chain Monte Carlo sampling, Environ Fluid Mech, 8, 579–595, https://doi.org/10.1007/s10652-008-9106-3, 2008.

Xu, T., Guo, Z., Xia, Y., Ferreira, V. G., Liu, S., Wang, K., Yao, Y., Zhang, X., and

Zhao, C.: Evaluation of twelve evapotranspiration products from machine learning, remote sensing and land surface models over conterminous United States, Journal of Hydrology, 578, 124105, https://doi.org/10.1016/j.jhydrol.2019.124105, 2019.

Yuan, K., Zhu, Q., Zheng, S., Zhao, L., Chen, M., Riley, W. J., Cai, X., Ma, H., Li, F., Wu, H., and Chen, L.: Deforestation reshapes land-surface energy-flux partitioning, Environ. Res. Lett., 16, 024014, https://doi.org/10.1088/1748-9326/abd8f9, 2021.

Zhang, K., Kimball, J. S., Nemani, R. R., and Running, S. W.: A continuous satellite-derived global record of land surface evapotranspiration from 1983 to 2006, Water Resources Research, 46, https://doi.org/10.1029/2009WR008800, 2010.

Zhu, G., Zhang, K., Li, X., Liu, S.-M., Ding, Z.-Y., Ma, J.-Z., Huang, C.-L., Han, T., and He, J.-H.: Evaluating the complementary relationship for estimating evapotranspiration using the multi-site data across north China, Agricultural and Forest Meteorology, 230–231, 33–44, https://doi.org/10.1016/j.agrformet.2016.06.006, 2016.

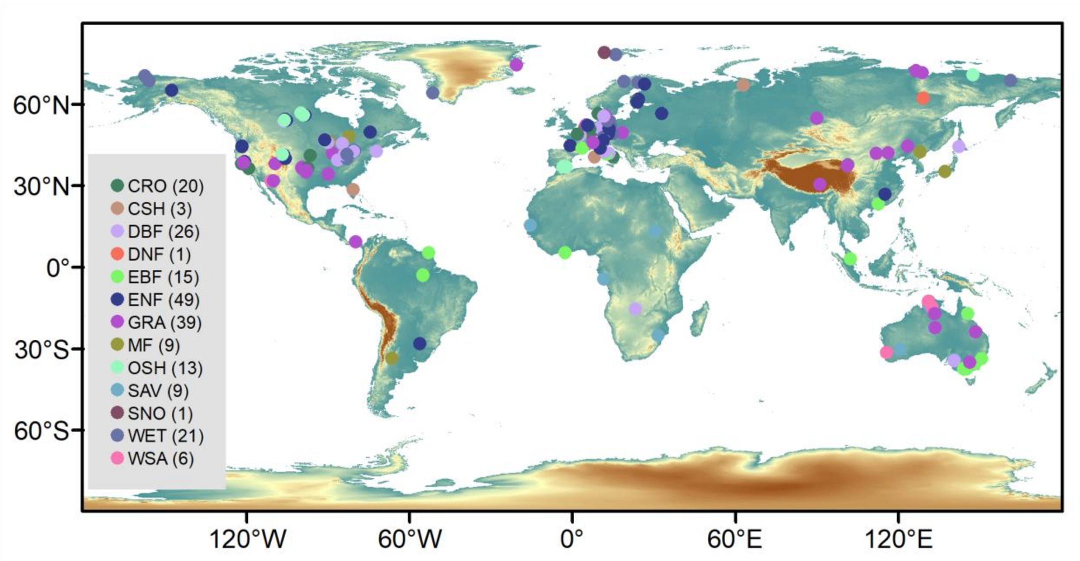

Fig. S1: Global spatial distribution of the 212 ET from FLUXNET and their corresponding vegetation types. Numbers in parentheses indicate the number of sites for each vegetation type (identified in Table S2).

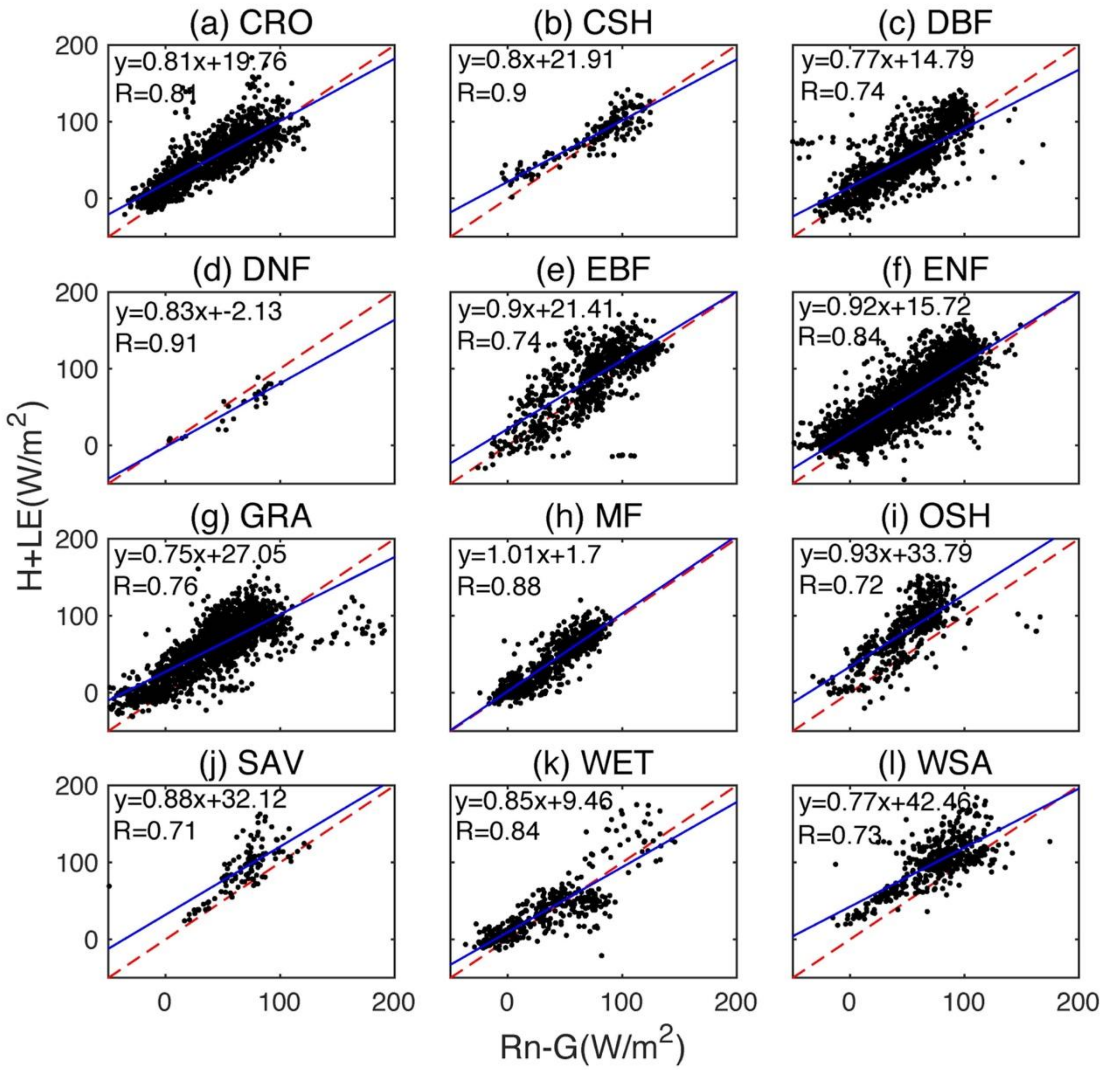

Fig. S2: Least-squares linear-regression-based energy balance closed scatter fit for monthly-scale flux tower data.

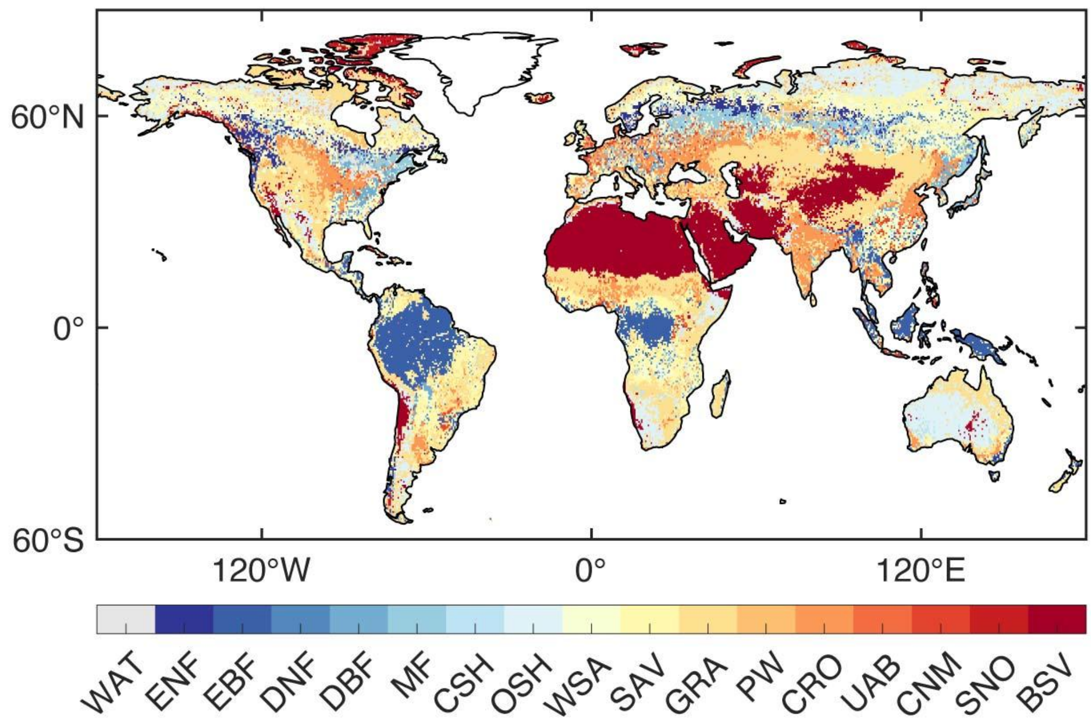

Fig. S3: Global spatial distribution of land cover types based on MOD12Q1.

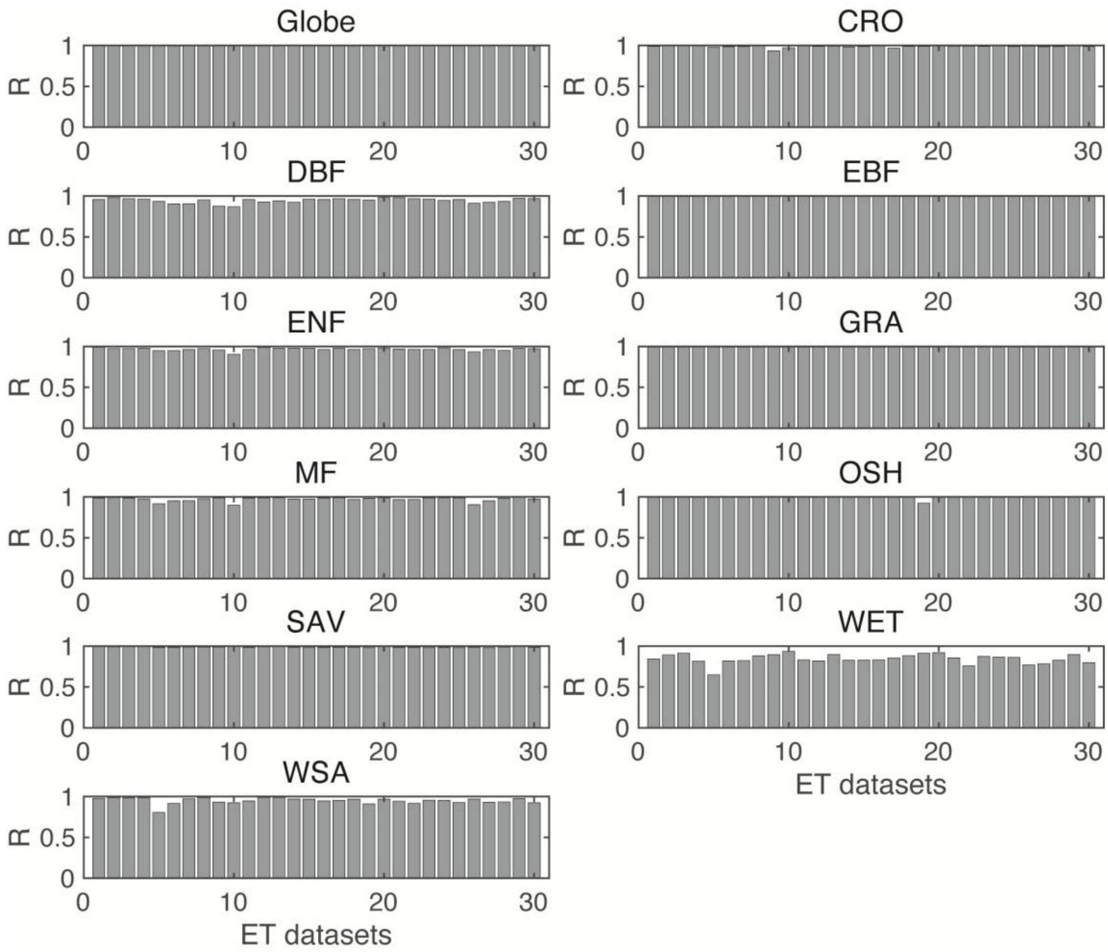

Fig. S4: Correlation coefficients for ET datasets at 1° and 0.5° spatial resolution globally and for each vegetation type.

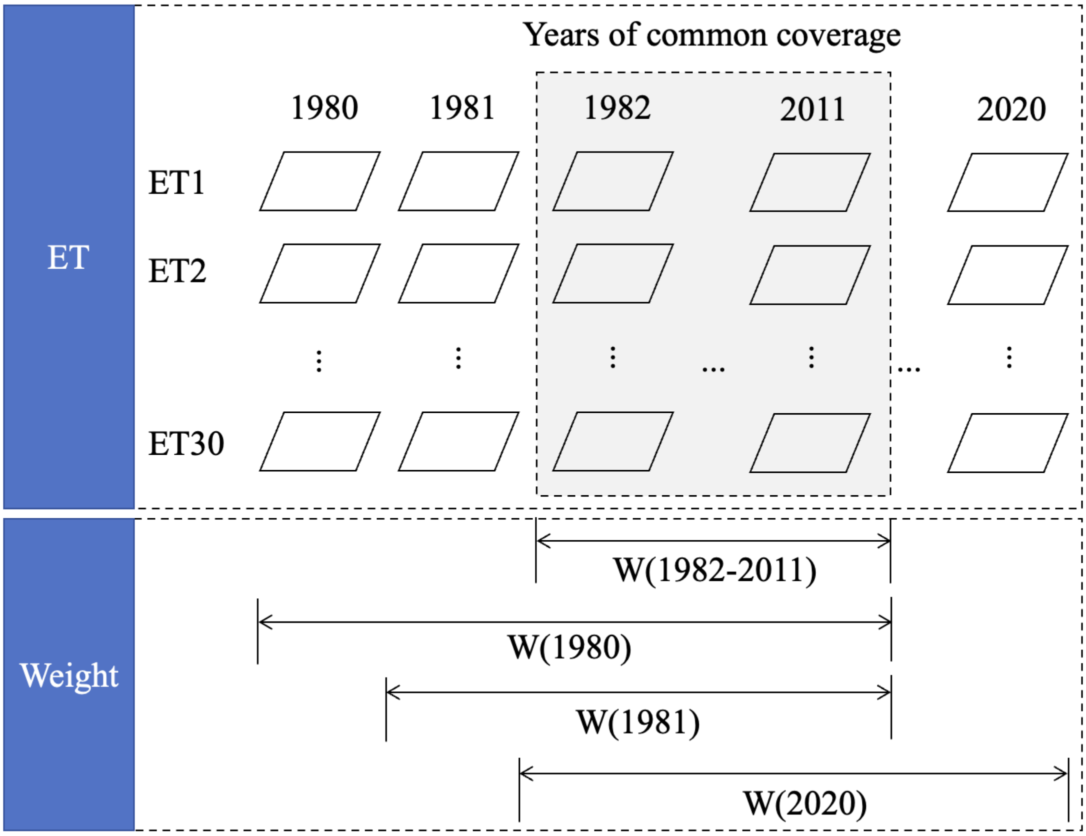

Fig. S5: Weighting scheme for ET datasets during the years with non-overlapping coverage.

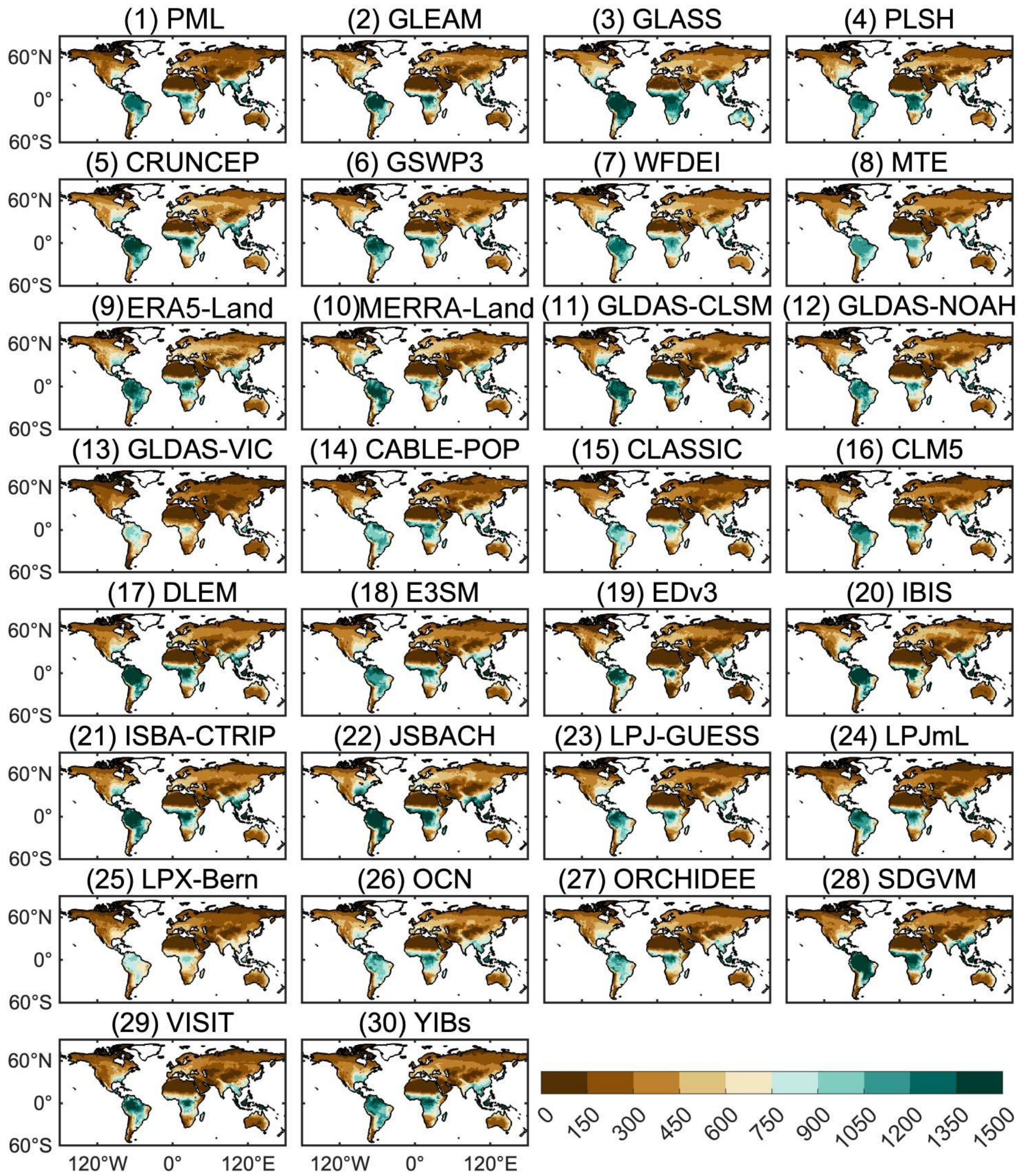

Fig. S6: Multi-year average evapotranspiration during 1982–2011 (unit: mm).

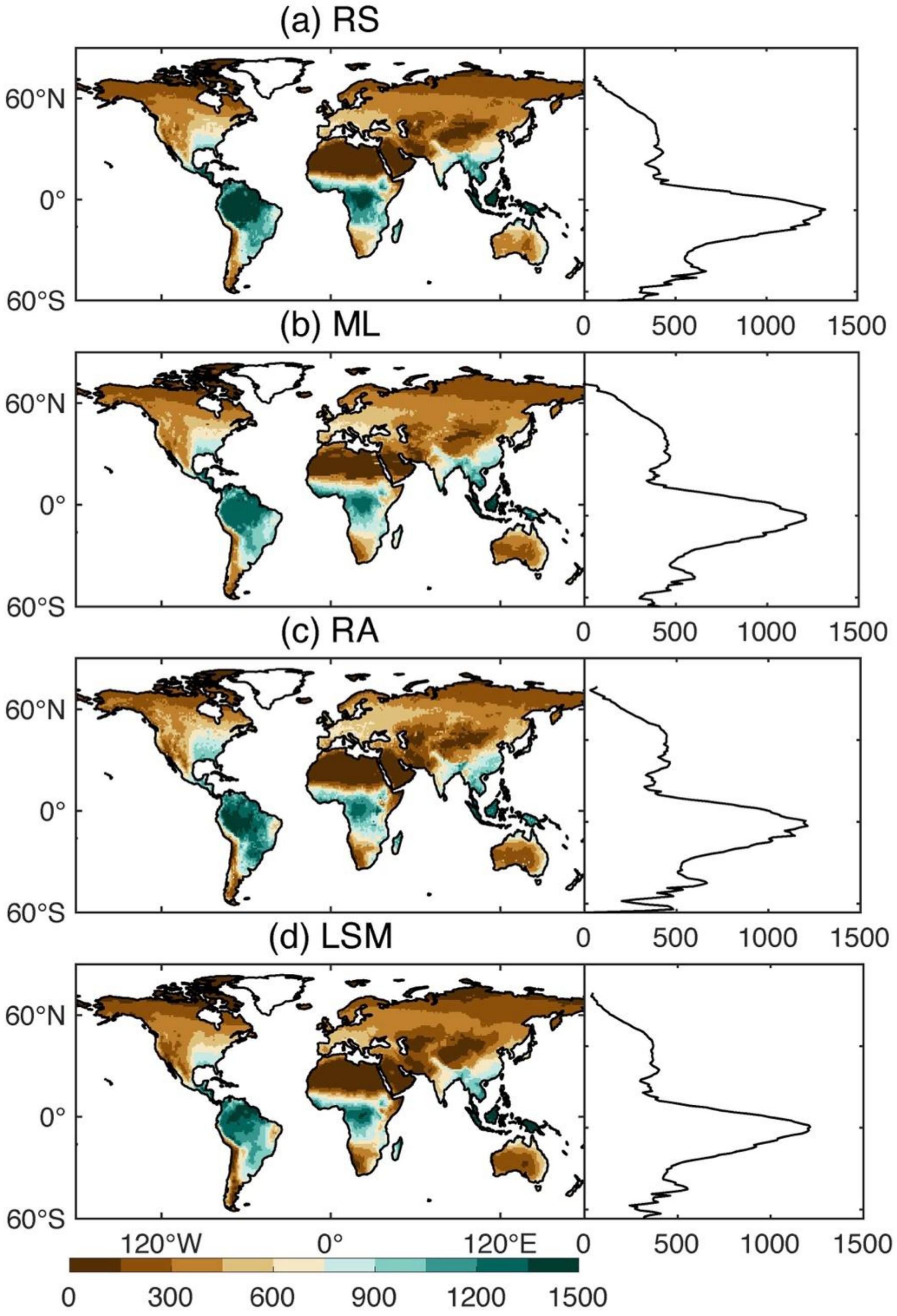

Fig. S7: Multi-year average evapotranspiration of multi-dataset median for four types of evapotranspiration datasets during 1982–2011 (unit: mm).

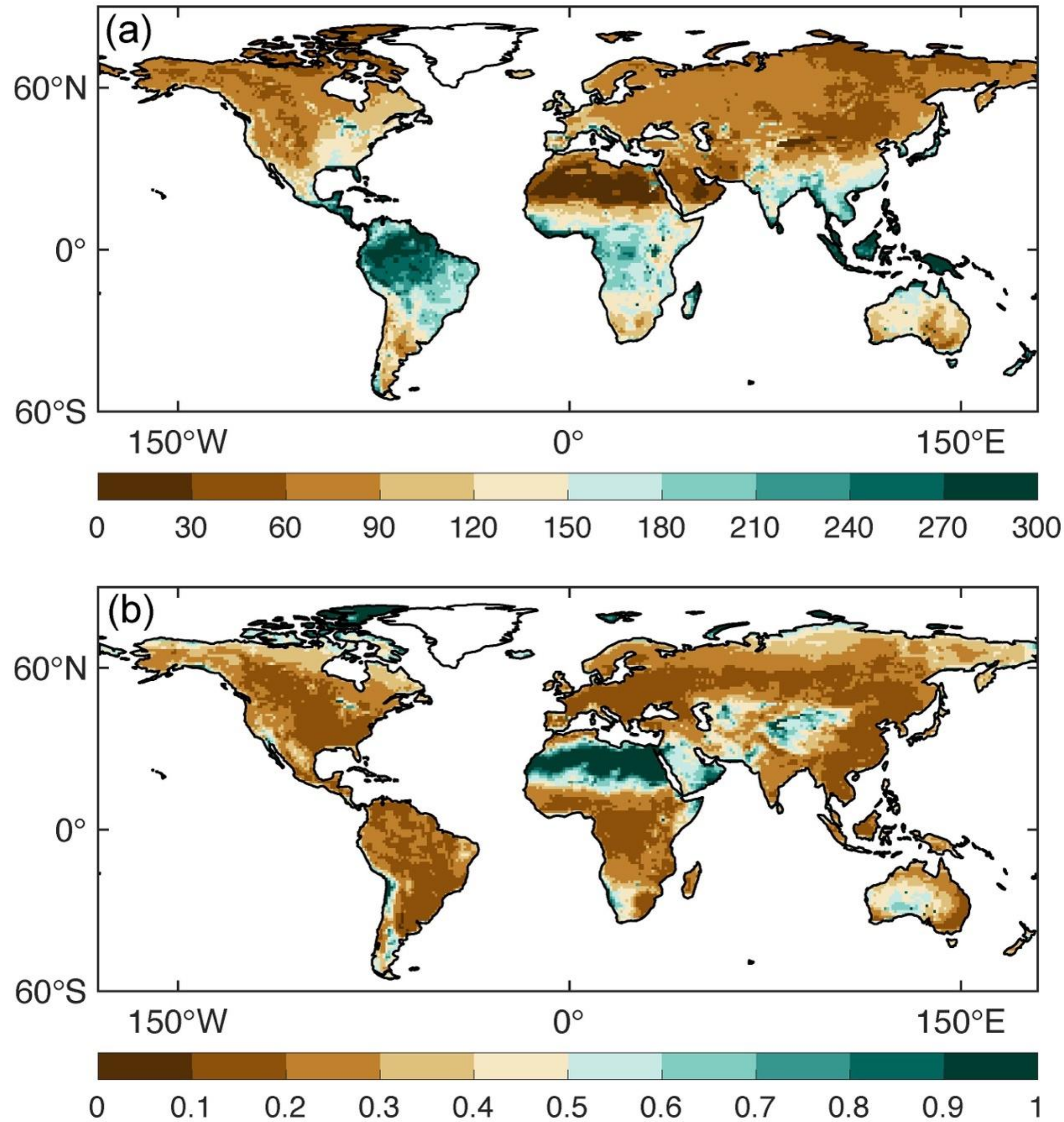

Fig. S8: (a) Standard deviation (STD) and (b) standardized standard deviation of 30 ET datasets at the multi-year average scale (unit: mm).

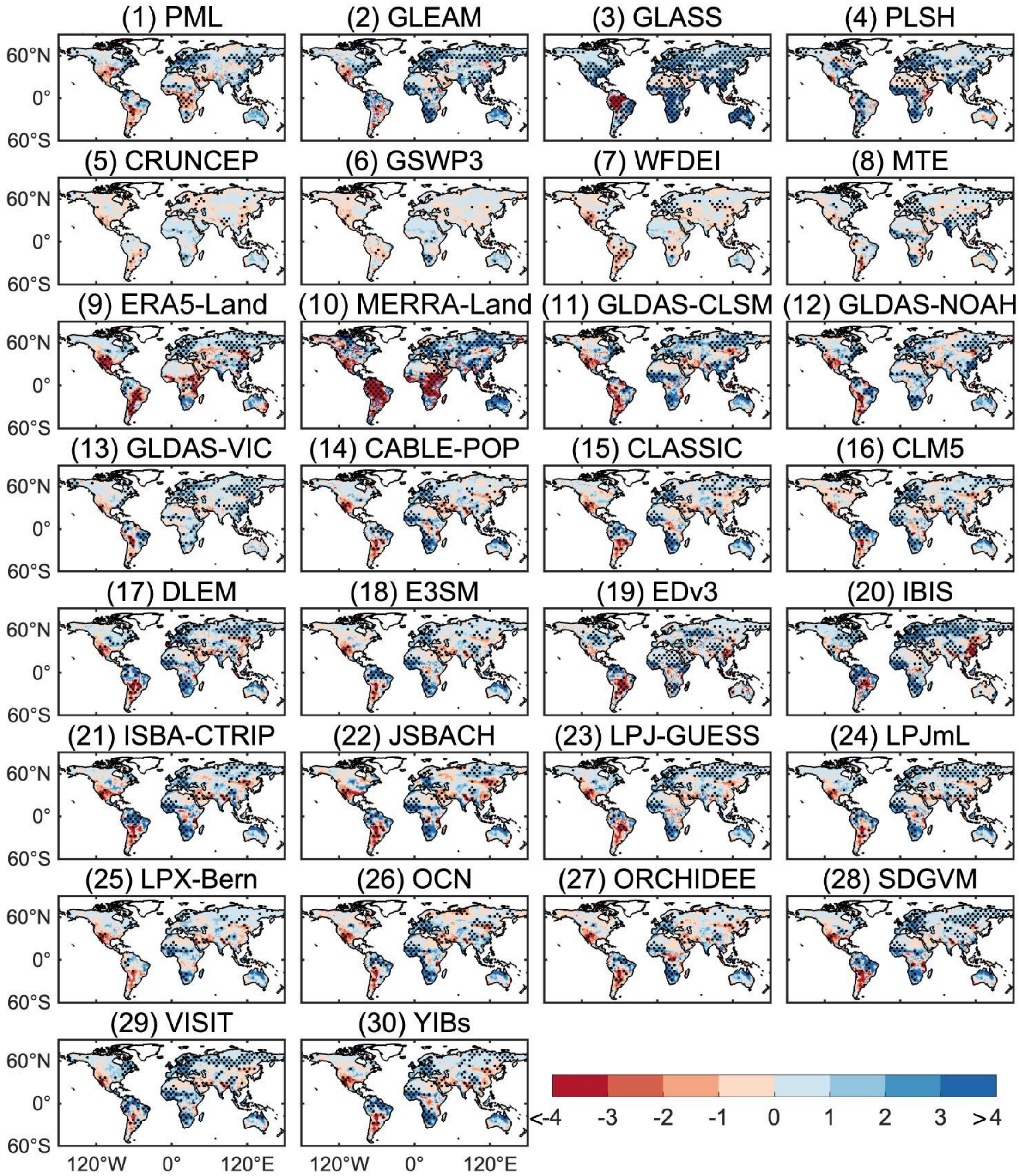

Fig. S9: Interannual trends in evapotranspiration datasets during 1982–2011 (unit: mm·yr^{-1}) (the black dotted areas indicate that the trend in these grid points was significant at the 95% level).

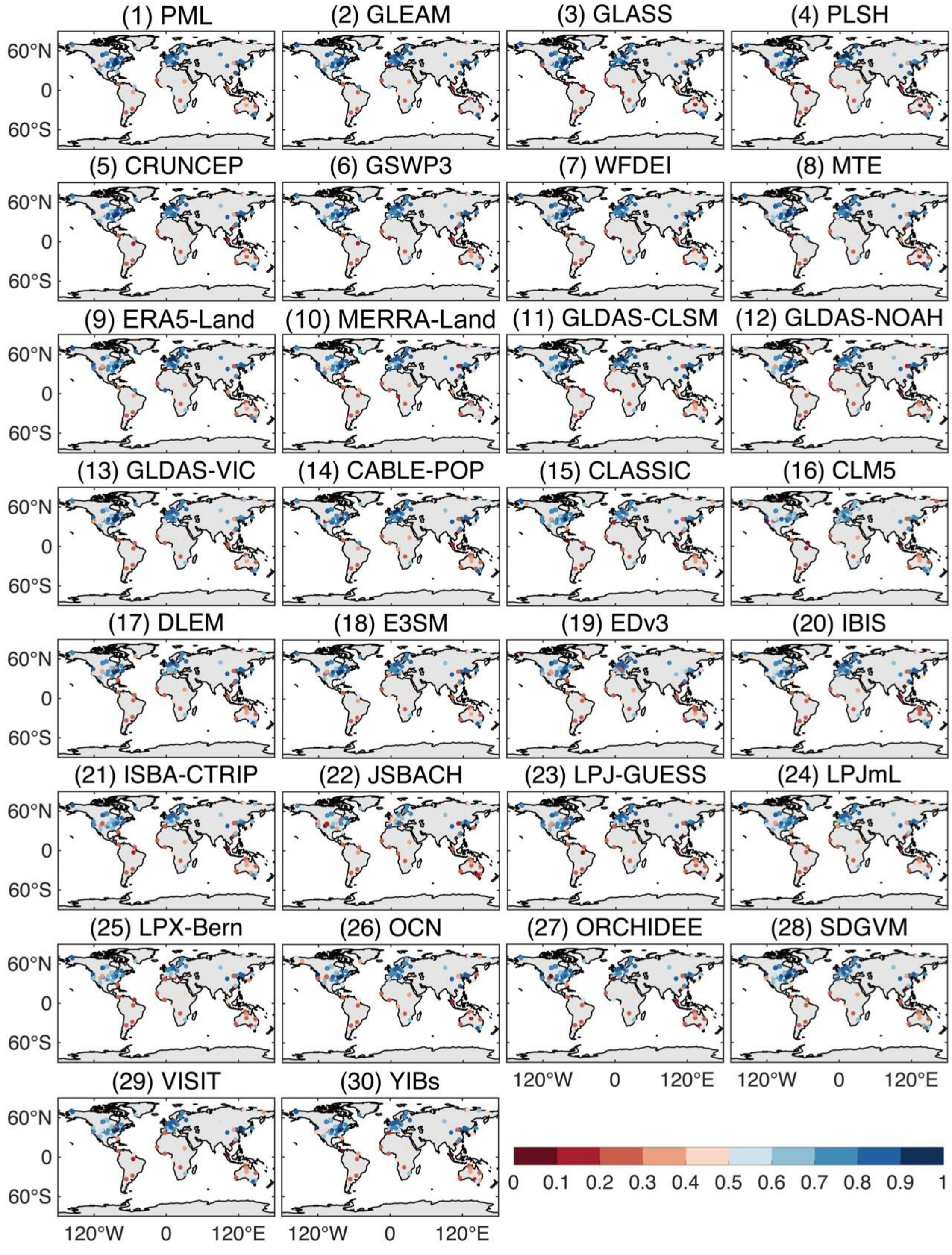

Fig. S10: Spatial distribution of correlation coefficients (R) for site validation of each ET dataset during 1991–2011.

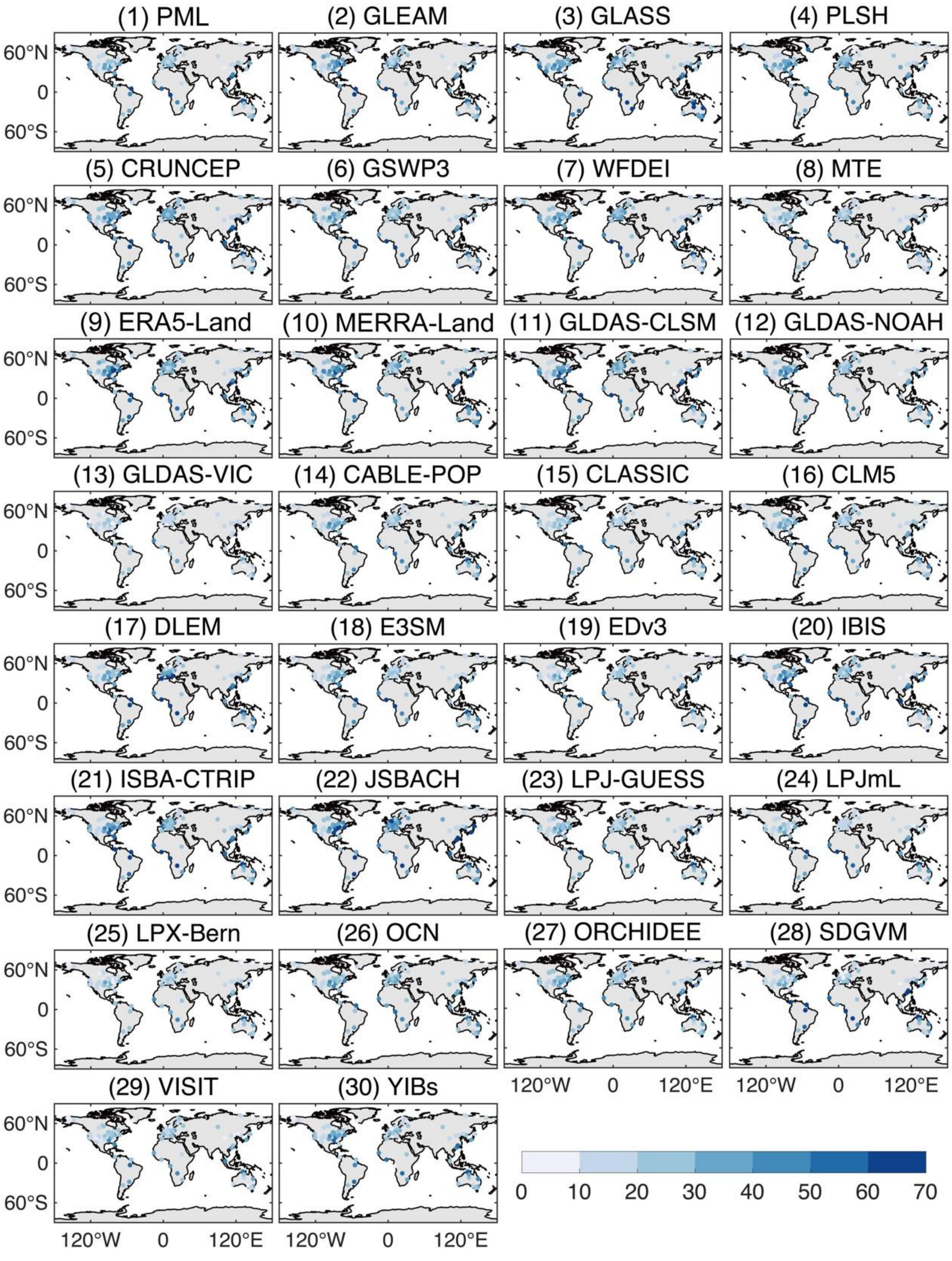

Fig. S11: Spatial distribution of mean absolute errors (MAE) for site validation of each ET dataset during 1991–2011.

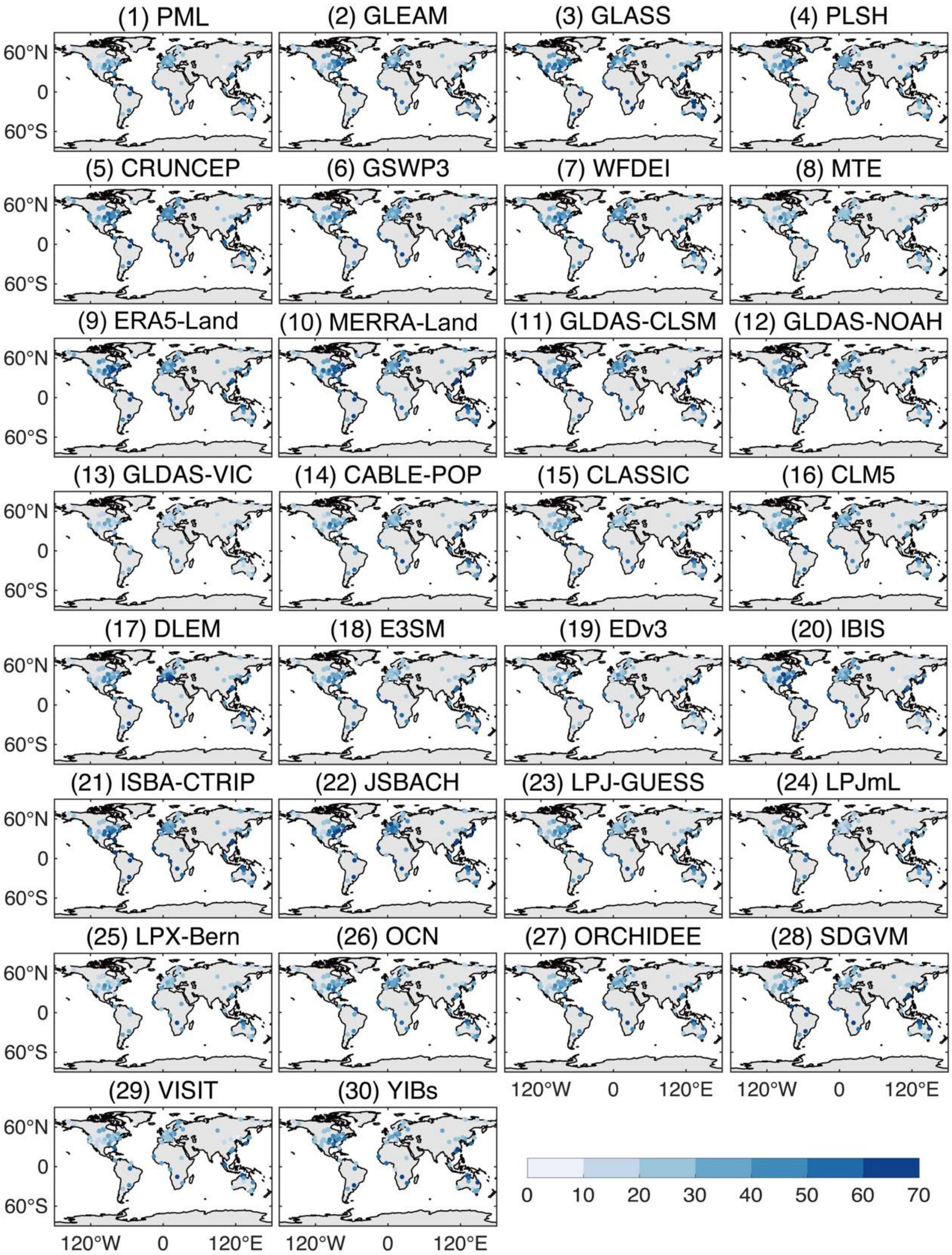

Fig. S12: Spatial distribution of root-mean-square errors (RMSE) for site validation of each ET dataset during 1991–2011.

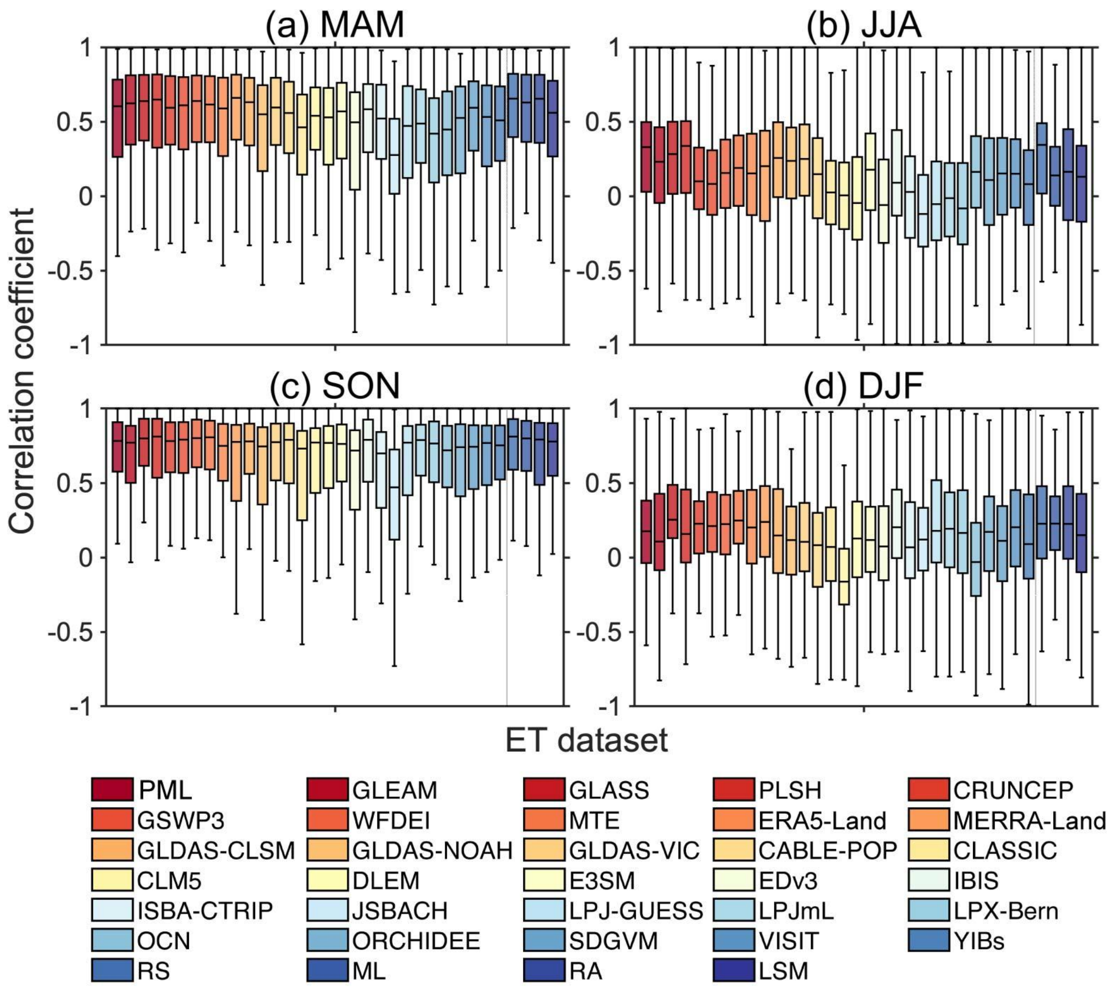

Fig. S13: Spatial distribution of seasonal correlation coefficients (R), validated at each ET dataset site, 1991–2011. (a) March–April–May (MAM), (b) June–July–August (JJA), (c) September–October–November (SON), (d) December–January–February (DJF). Each box-and-whisker plot represents the range of uncertainty across sites (for each box, the central horizontal line represents the median of the sample, the upper and lower boundaries represent the 75th and 25th percentile values, respectively, and the two 'whiskers' extend to the maximum and minimum values that are not considered outliers, which are plotted separately).

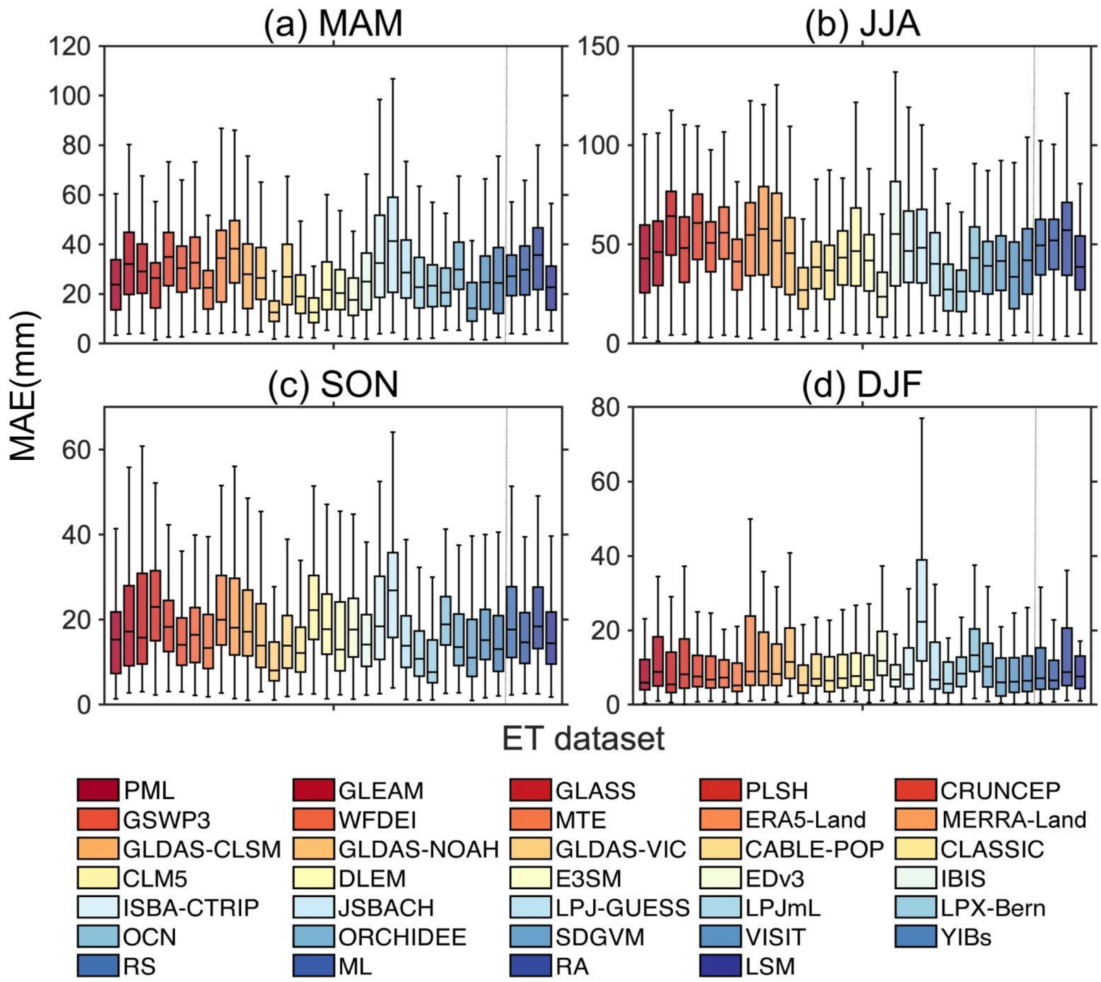

Fig. S14: Spatial distribution of seasonal mean absolute errors (MAE) in the validation of each ET dataset site, 1991–2011. (a) March–April–May (MAM), (b) June–July–August (JJA), (c) September–October–November (SON), (d) December–January–February (DJF). Each box-and-whisker plot represents the range of uncertainty across sites (for each box, the central horizontal line represents the median of the sample, the upper and lower boundaries represent the 75th and 25th percentile values, respectively, and the two 'whiskers' extend to the maximum and minimum values that are not considered outliers, which are plotted separately).

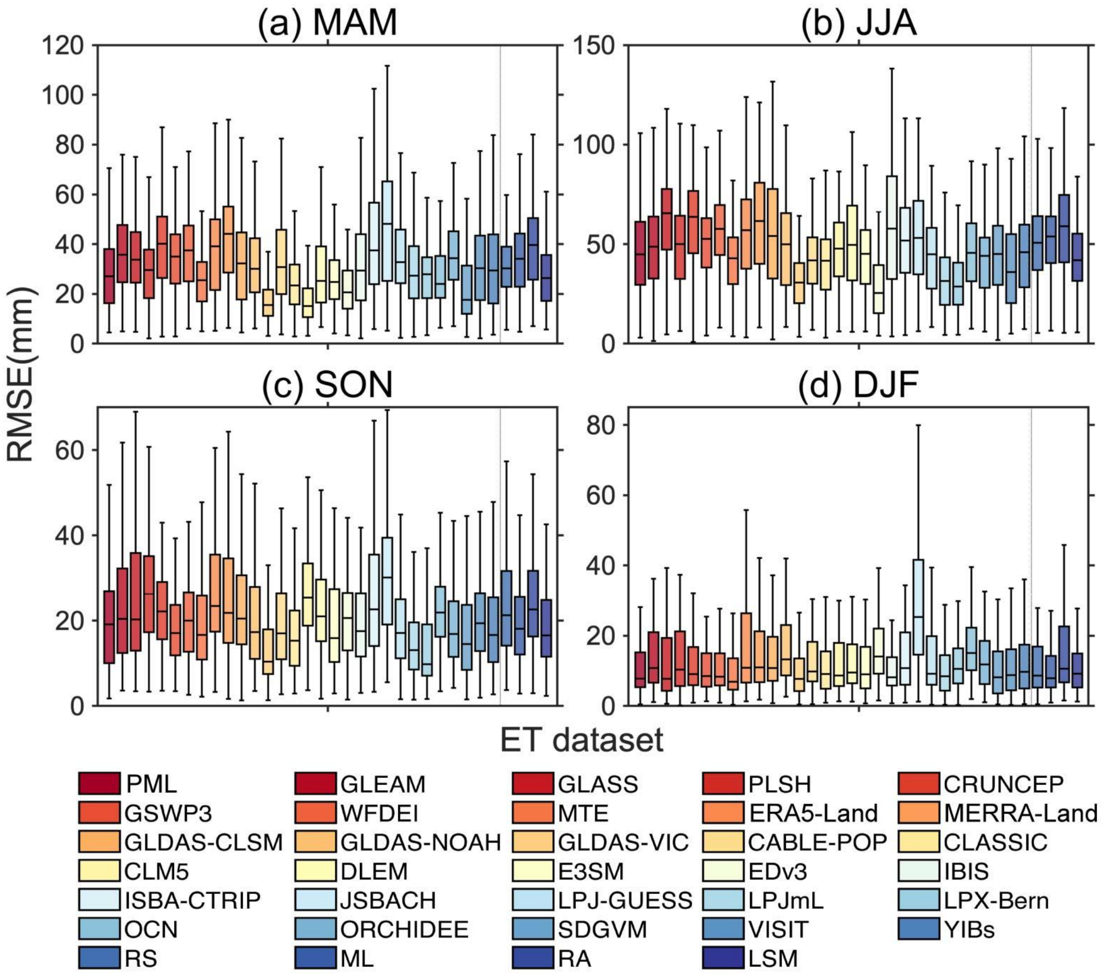

Fig. S15: Spatial distribution of seasonal root-mean-square errors (RMSE) validated at each ET dataset site for 1991–2011. (a) March–April–May (MAM), (b) June–July–August (JJA), (c) September–October–November (SON), (d) December–January–February (DJF). Each box-and-whisker plot represents the range of uncertainty across sites (for each box, the central horizontal line represents the median of the sample, the upper and lower boundaries represent the 75th and 25th percentile values, respectively, and the two 'whiskers' extend to the maximum and minimum values that are not considered outliers, which are plotted separately).

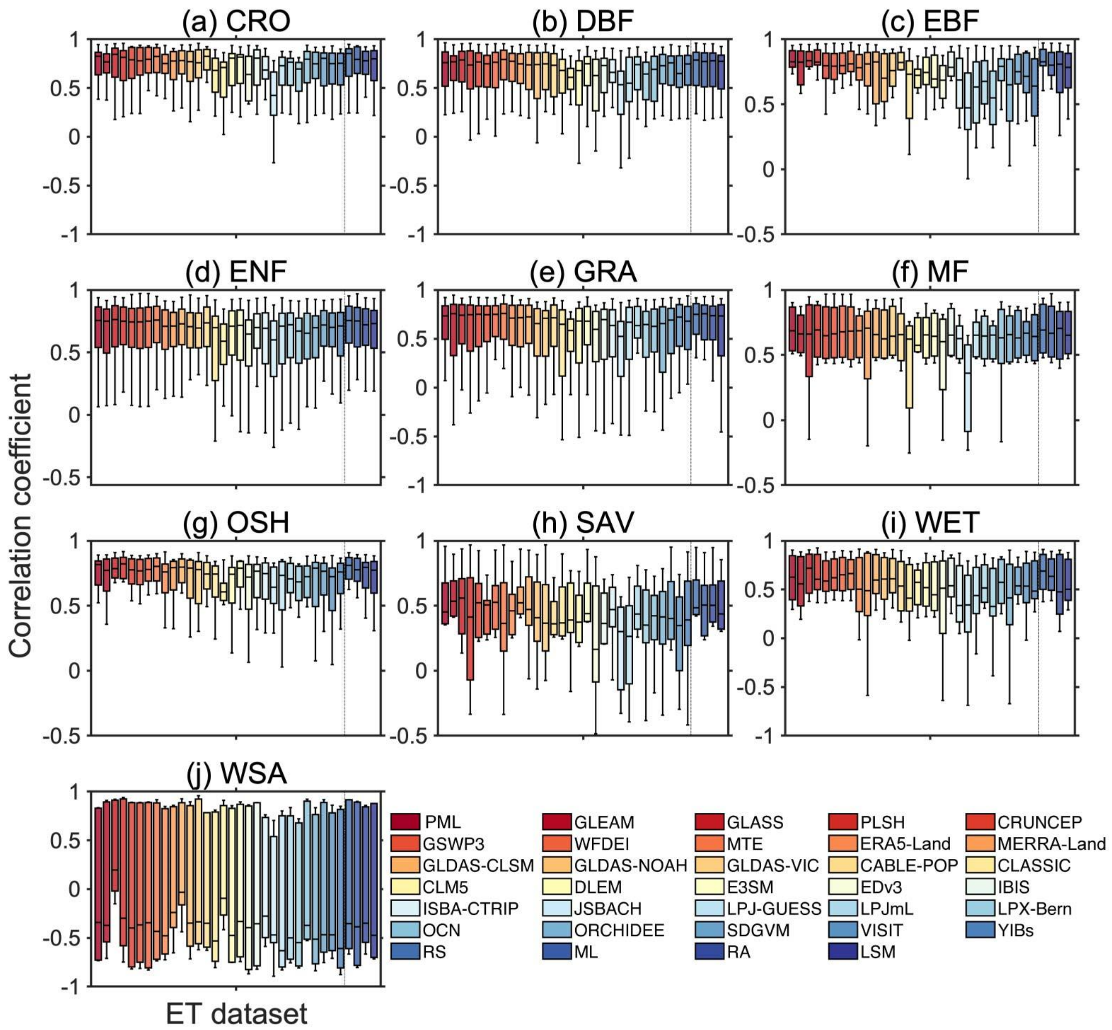

Fig. S16: Correlation coefficients (R) between each ET dataset and ET from FLUXNET for different vegetation types, 1991–2011. Each box-and-whisker plot indicates the range of uncertainty for the different sites (for each box, the central horizontal line indicates the median of the sample, its upper and lower boundaries indicate the 75th and 25th percentile values, respectively, and the two 'whiskers' extend to the maximum and minimum values that are not considered outliers, and outliers are plotted separately).

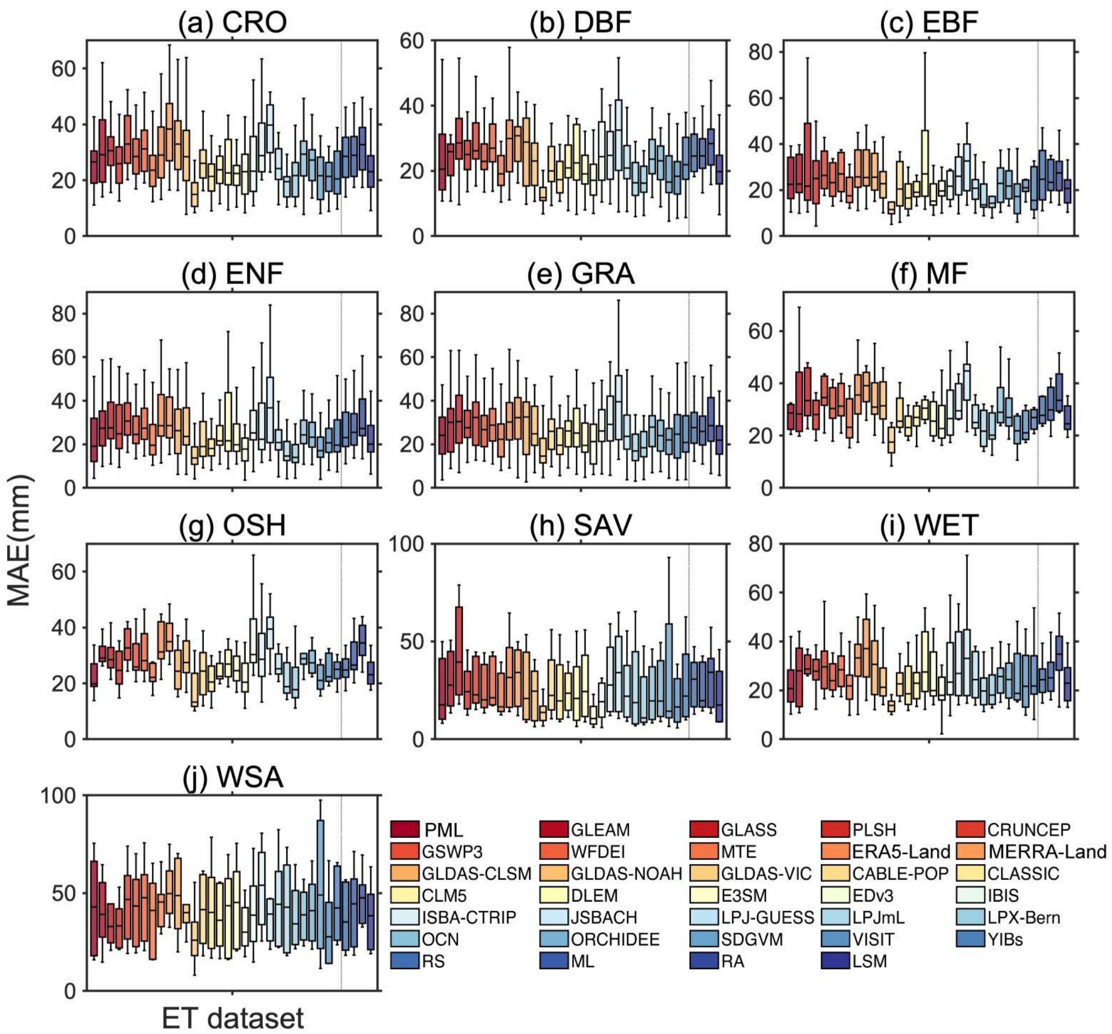

Fig. S17: Mean absolute errors (MAE) for each ET dataset and ET from FLUXNET across vegetation types, 1991–2011. Each box-and-whisker plot represents the range of uncertainty for the different sites (for each box, the central horizontal line represents the median of the sample, the upper and lower borders represent the 75th and 25th percentile values, respectively, and the two ‘whiskers’ extend to the maximum and minimum values that are not considered outliers, which are plotted separately).

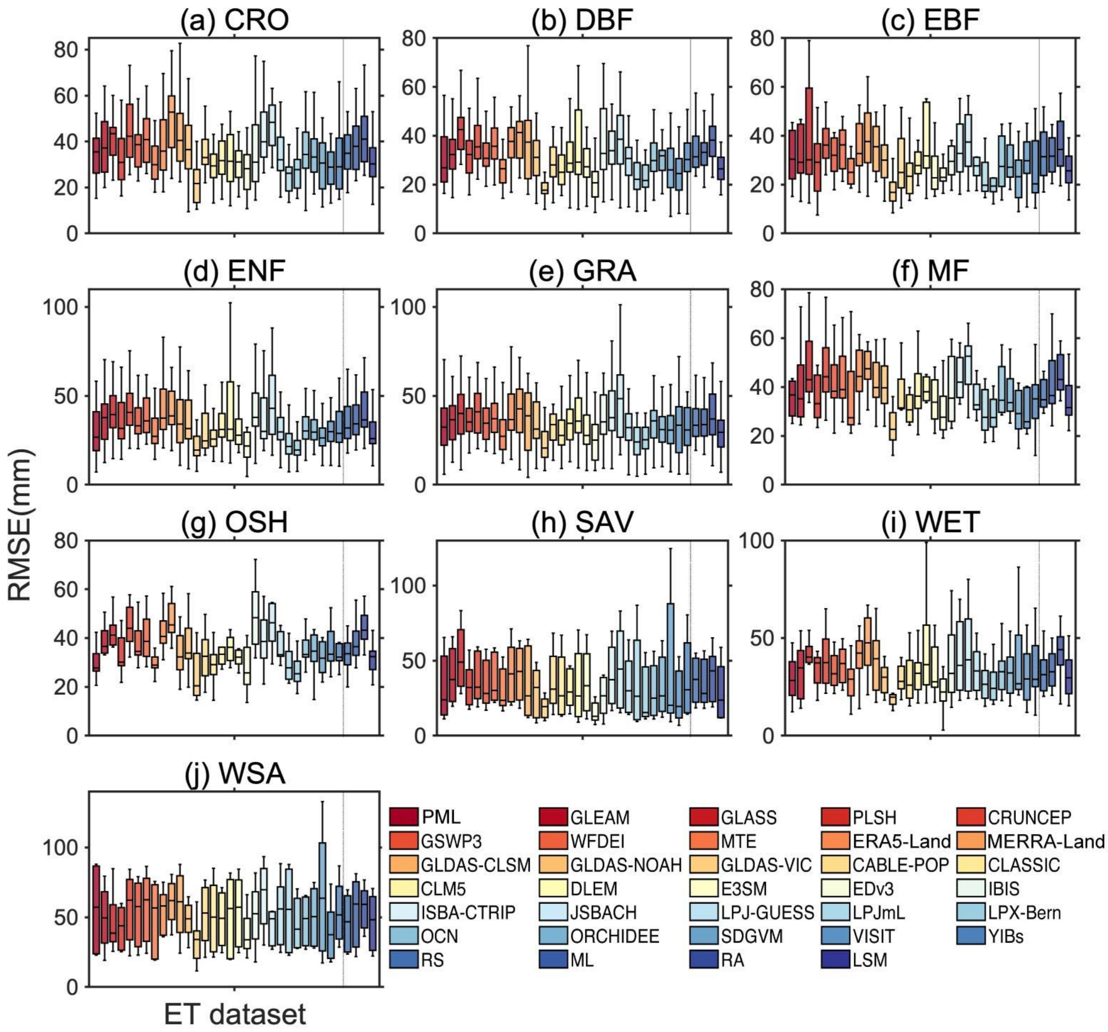

Fig. S18: Root-mean-square errors (RMSE) for each ET dataset and ET from FLUXNET for different vegetation types, 1991–2011. Each box-and-whisker plot represents the range of uncertainty for the different sites (for each box, the central horizontal line represents the median of the sample, the upper and lower boundaries represent the 75th and 25th percentile values, respectively, and the two 'whiskers' extend to the maximum and minimum values that are not considered outliers, which are plotted separately).

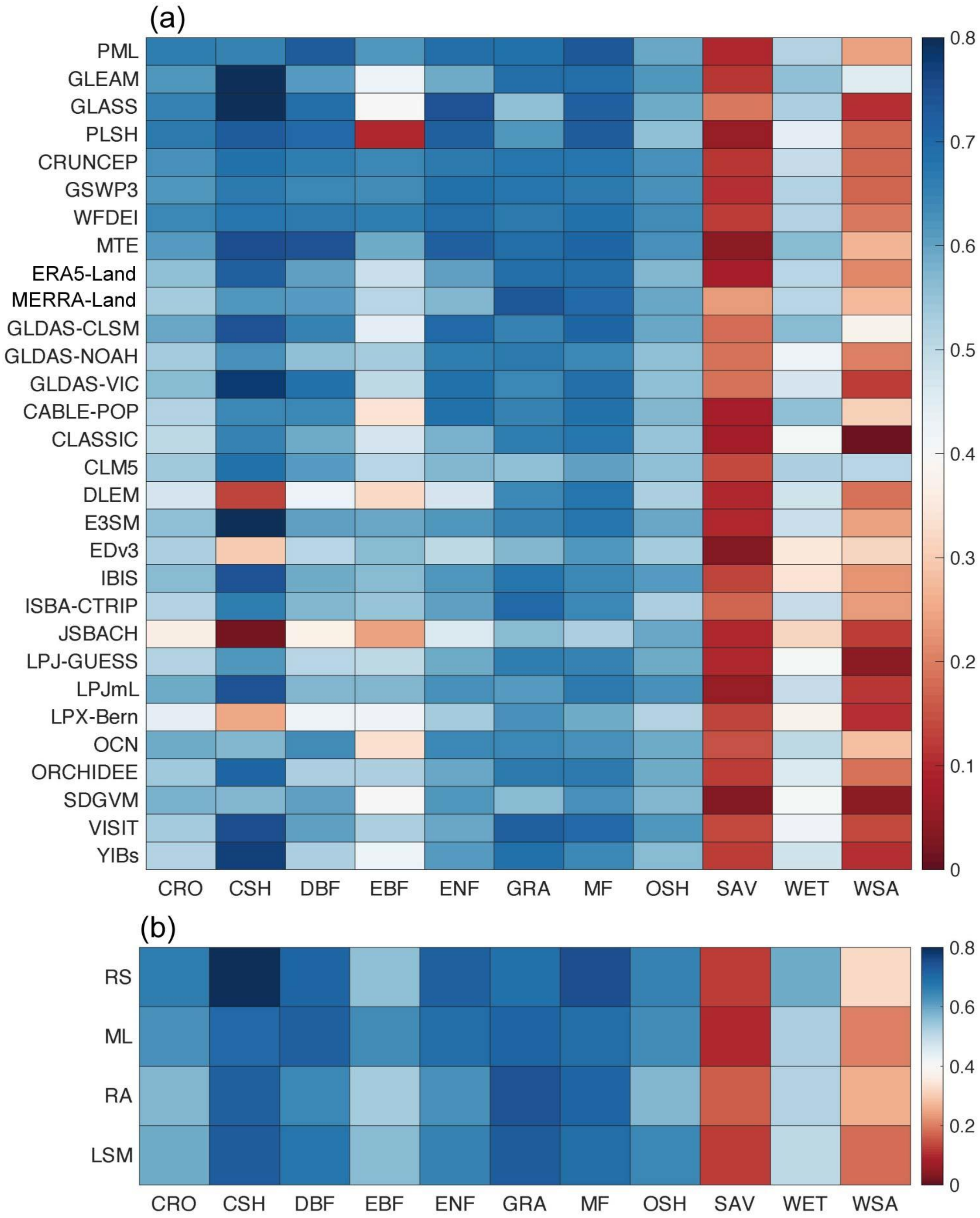

Fig. S19: Correlation coefficients between monthly values of ET datasets and ET from FLUXNET for 12 vegetation types during 1991–2011.

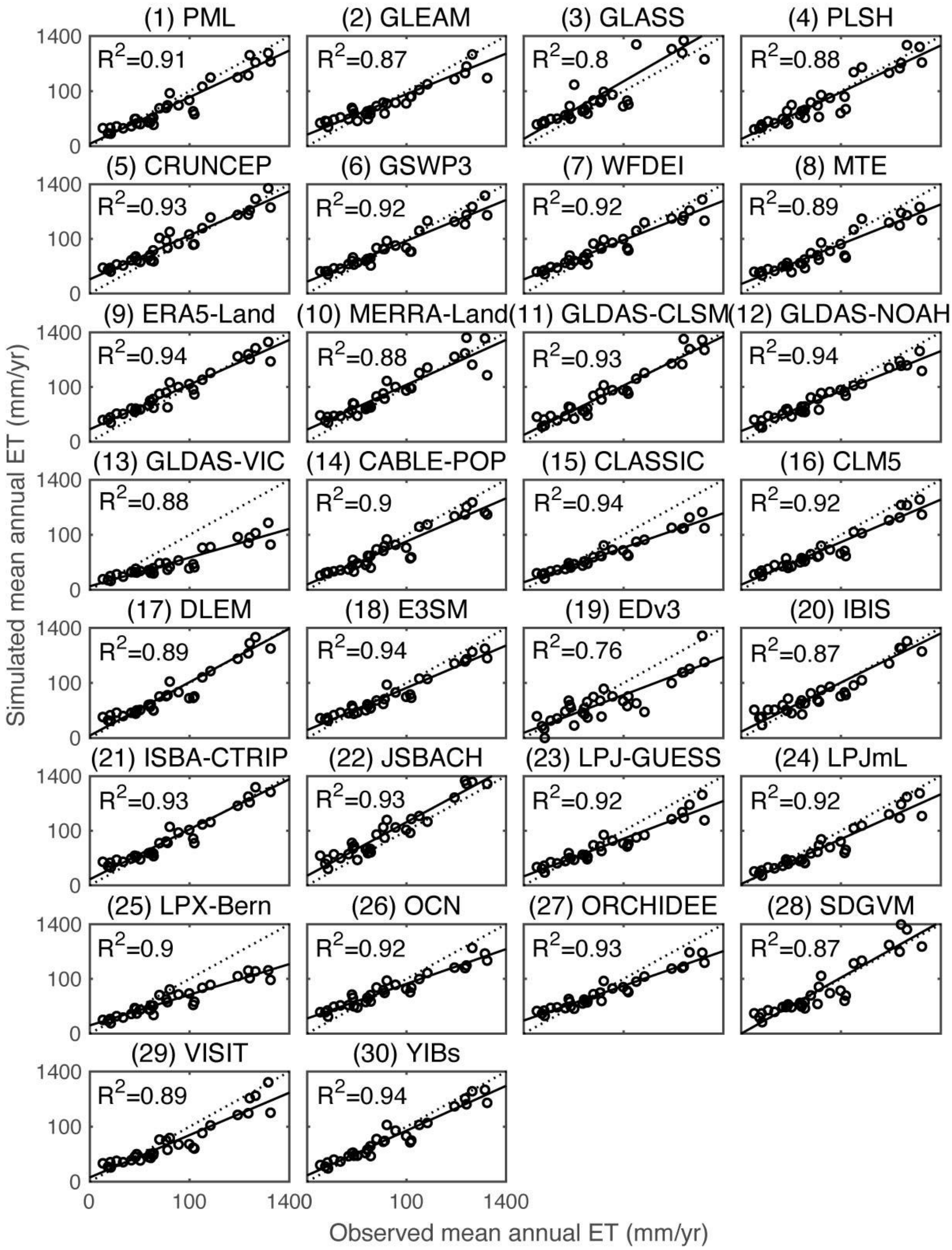

Fig. S20: Comparison of multi-year average evapotranspiration from 30 ET datasets and multi-year average observed evapotranspiration from basin water balance. Each small circle in the figure represents a basin.

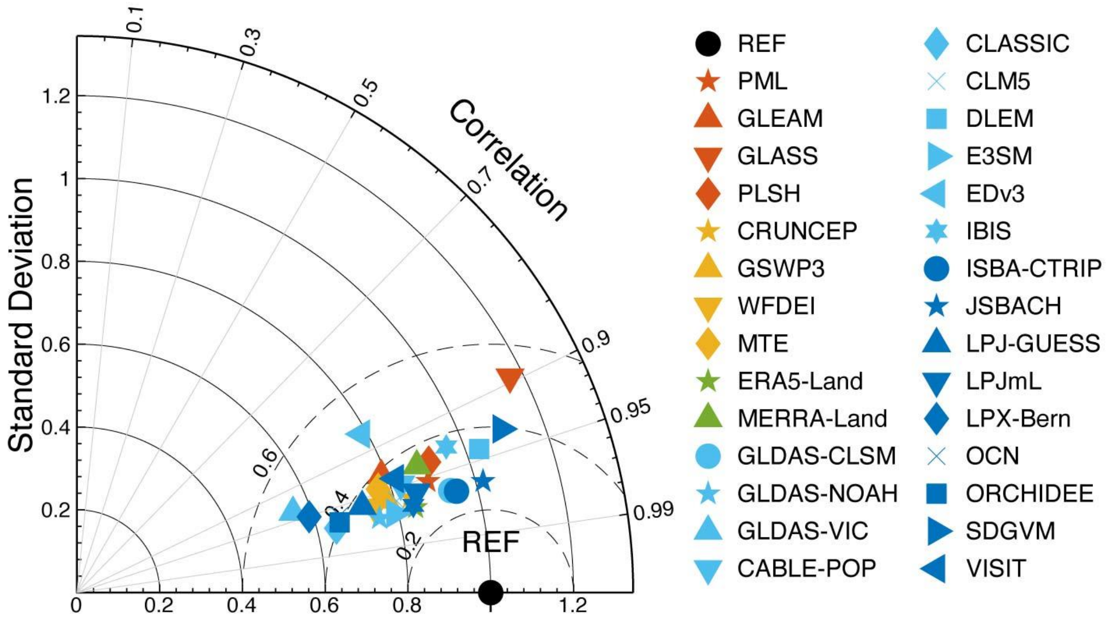

Fig. S21: Overall accuracy of simulated basin-scale evapotranspiration for all ET datasets.

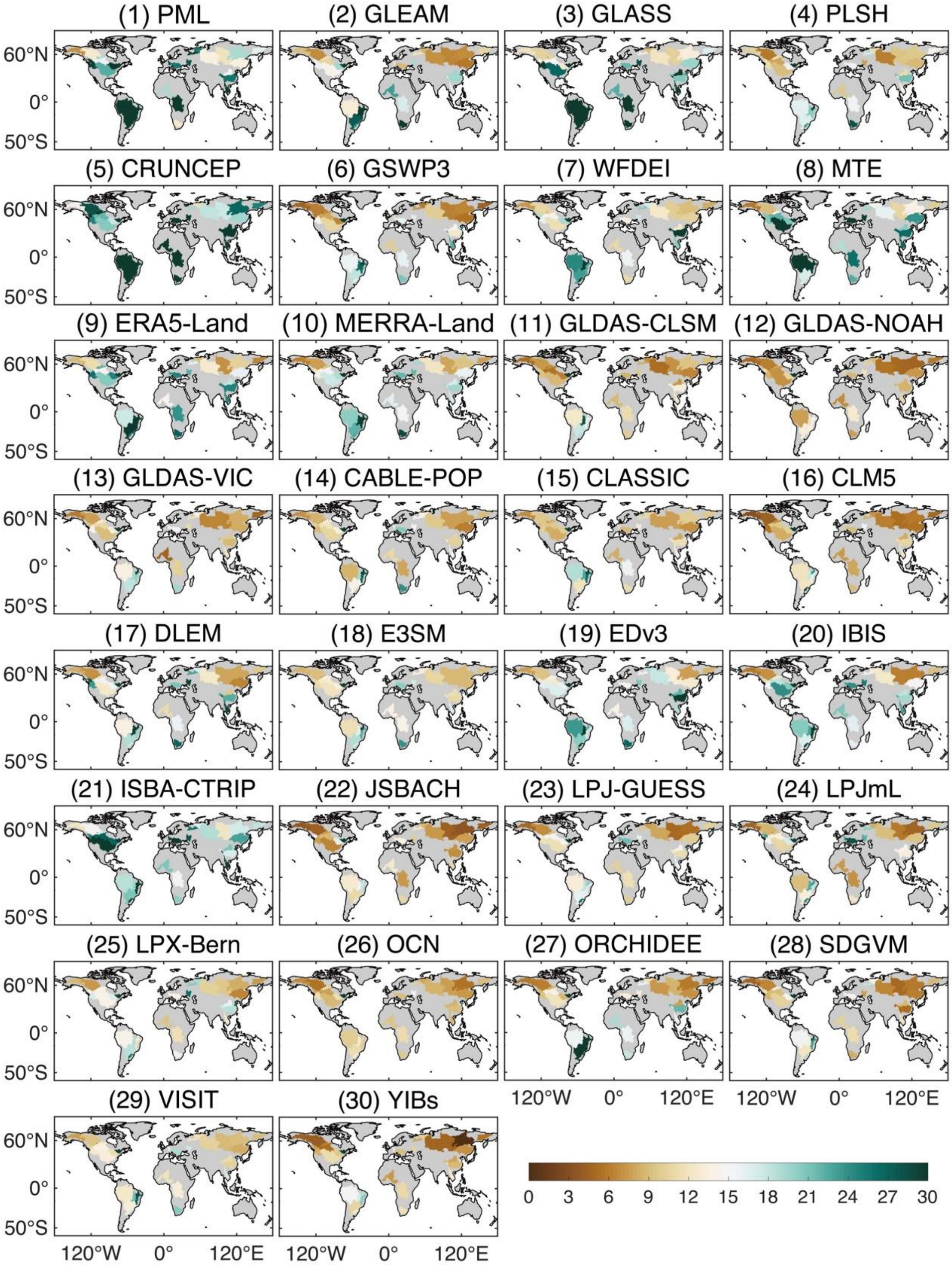

Fig. S22: Spatial distribution of TCH uncertainty for 32 basins globally during 1982–2011 (unit: mm).

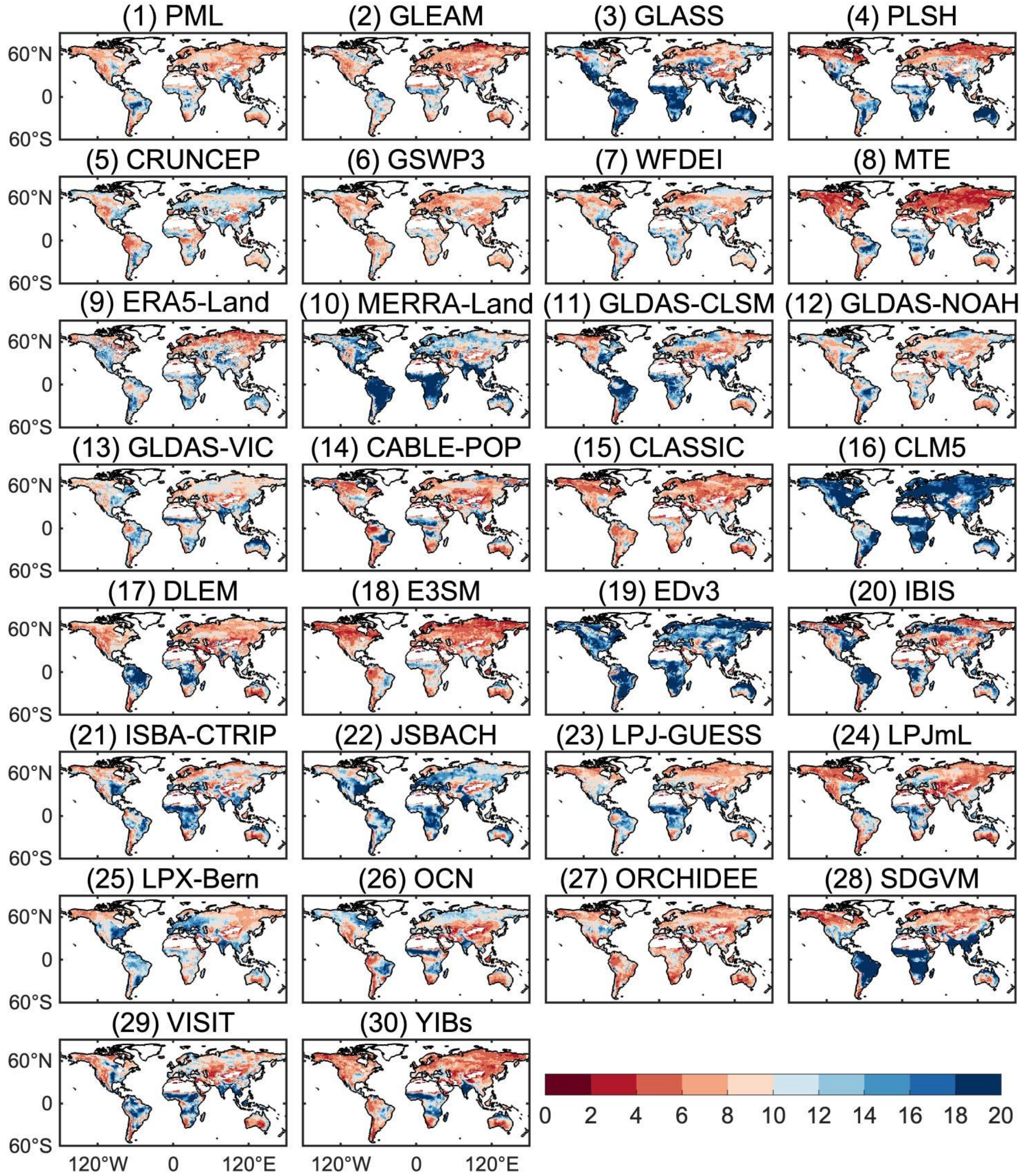

Fig. S23: Spatial distribution of uncertainty of TCH for each ET dataset on monthly scale for the common coverage years from 1982 to 2011 (unit: mm).

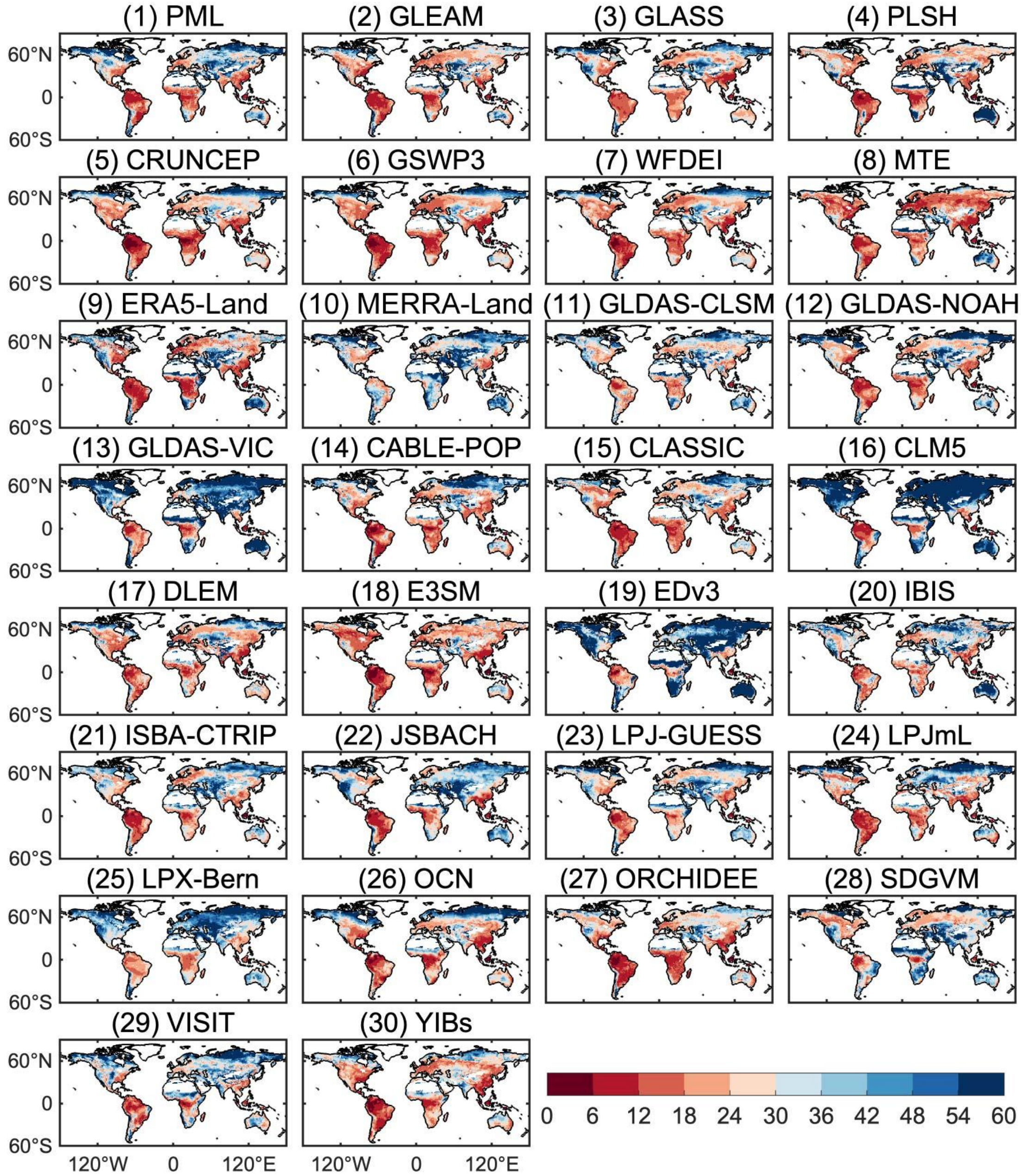

Fig. S24: Spatial distribution of relative uncertainty of TCH for each ET dataset on monthly scale for the common coverage years from 1982 to 2011 (unit: %).

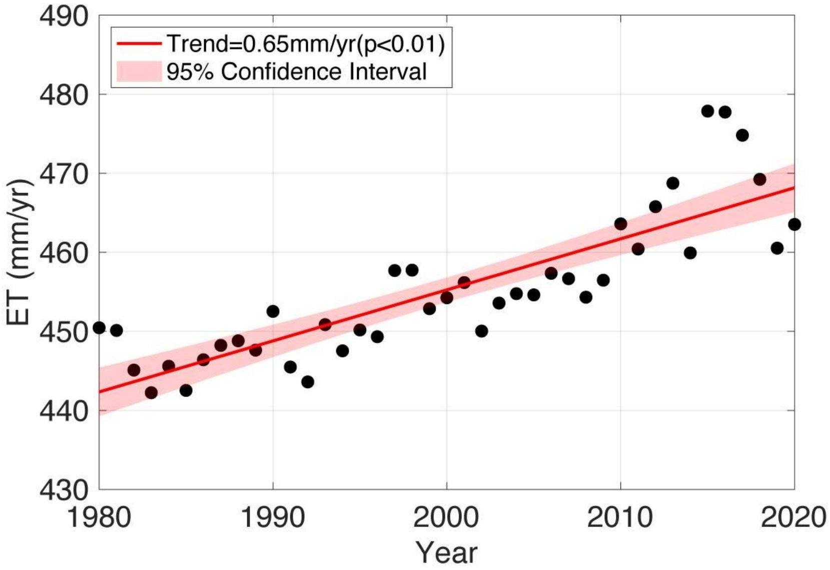

Fig. S25: Interannual variations of BMA-ET during 1980–2020. The global land average results are calculated based on a weighted average of the global land area.

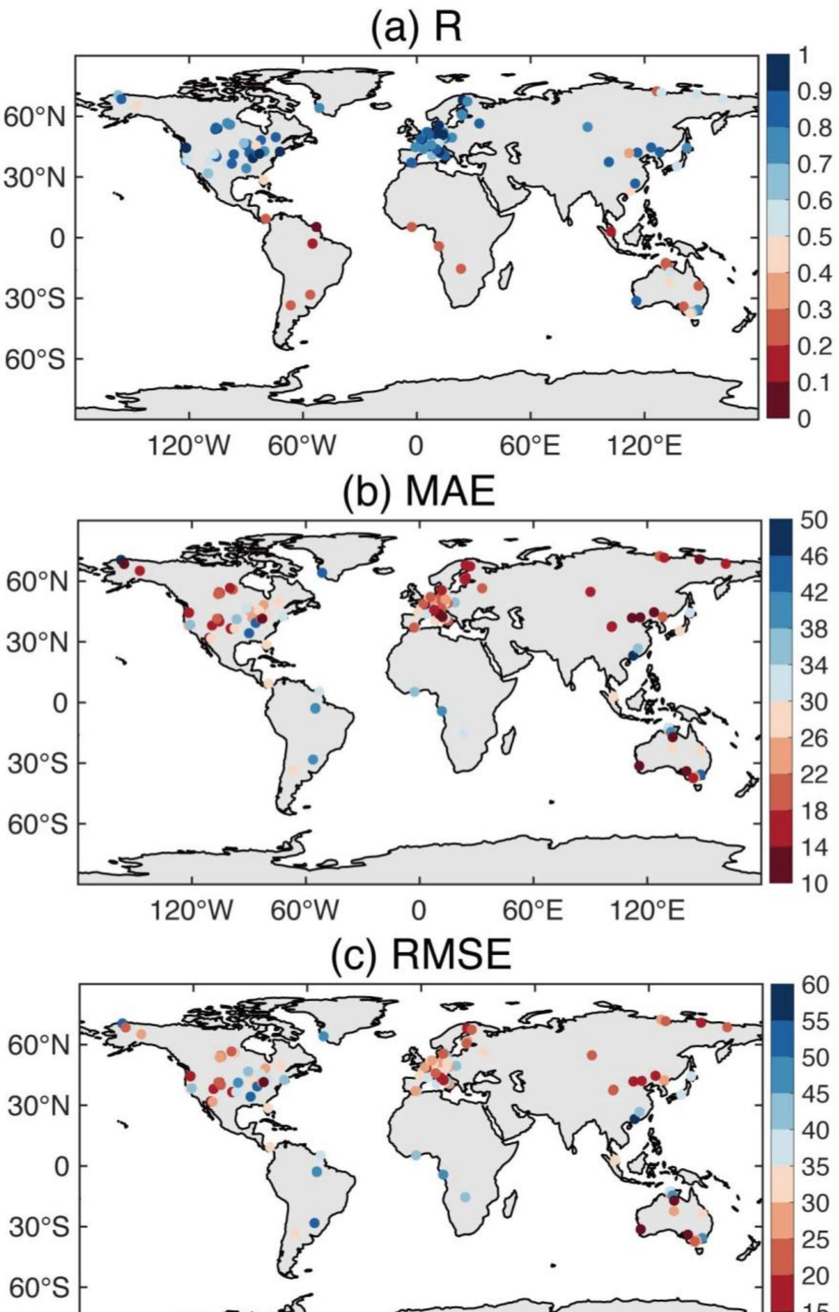

Fig. S26: Spatial distribution of correlation coefficient (R), mean absolute error (MAE) and root mean square error (RMSE) verified by BMA-ET and ET from FLUXNET from 1991 to 2011.

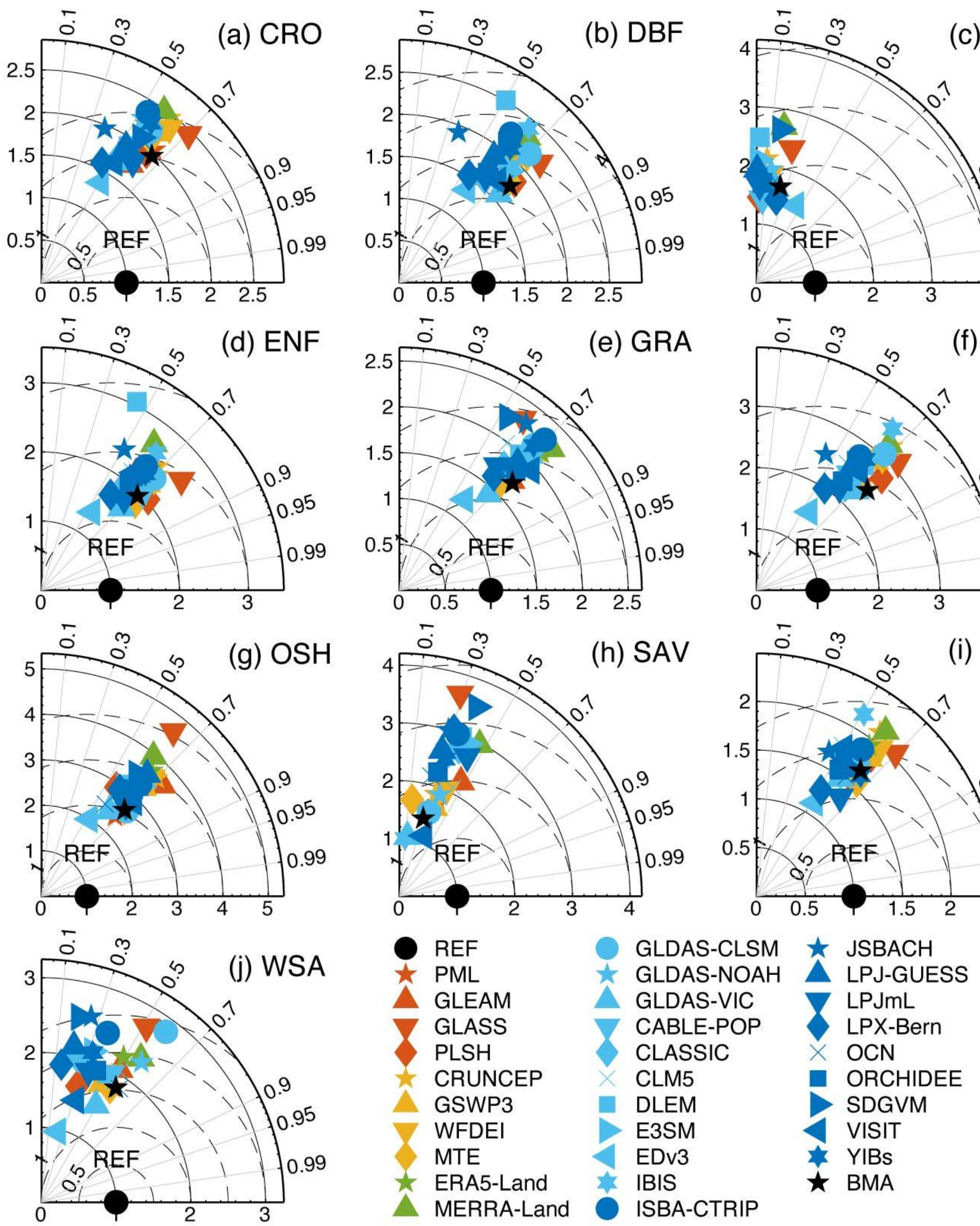

Fig. S27: Taylor diagram of ET datasets and BMA-ET at all sites under different vegetation types at monthly scale from 1991 to 2011. The observation data is ET from FLUXNET2015.

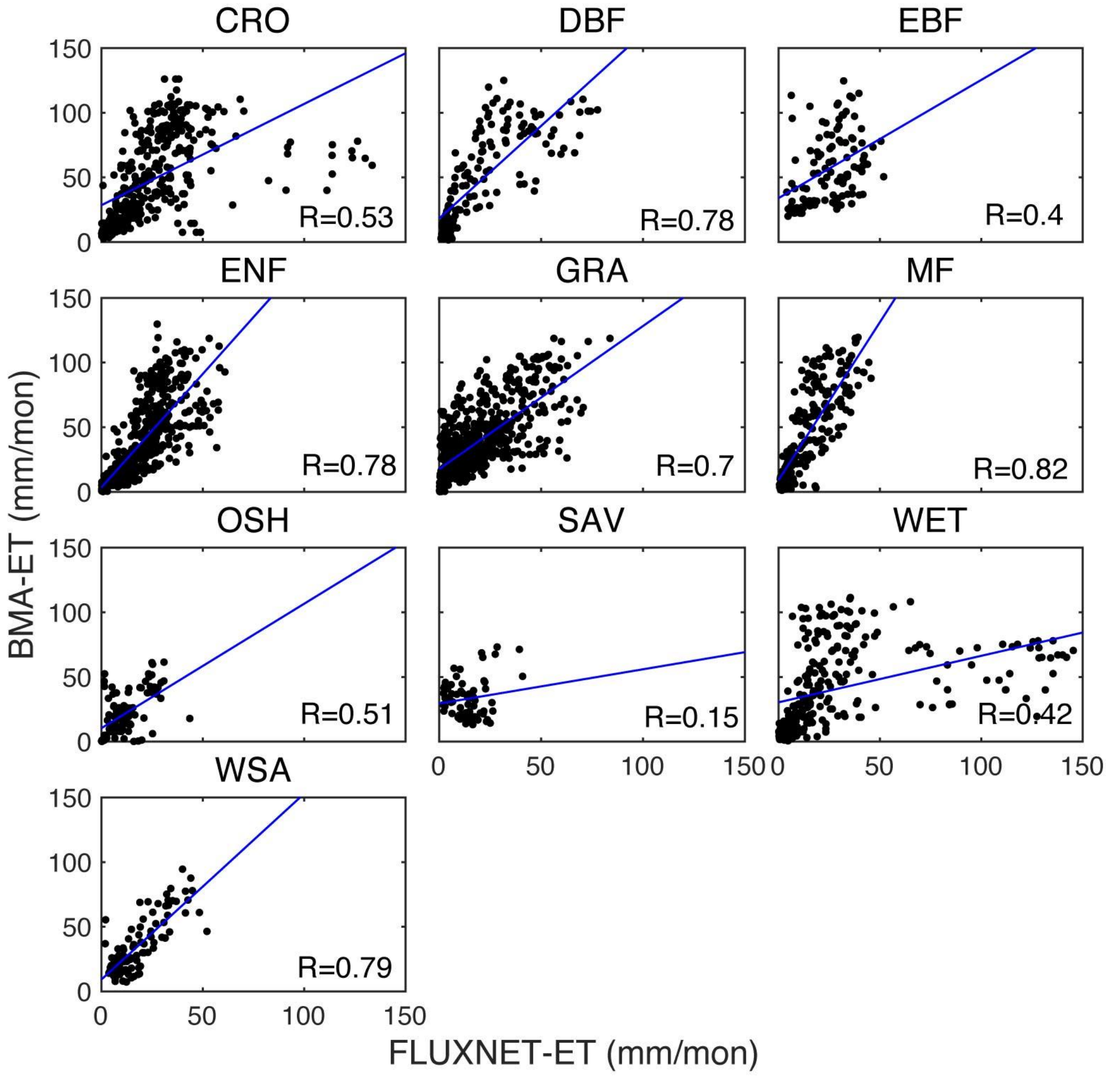

Fig. S28: Accuracy evaluation of BMA-ET under different vegetation types during the period 2012–2015. The observation data is ET from FLUXNET2015.

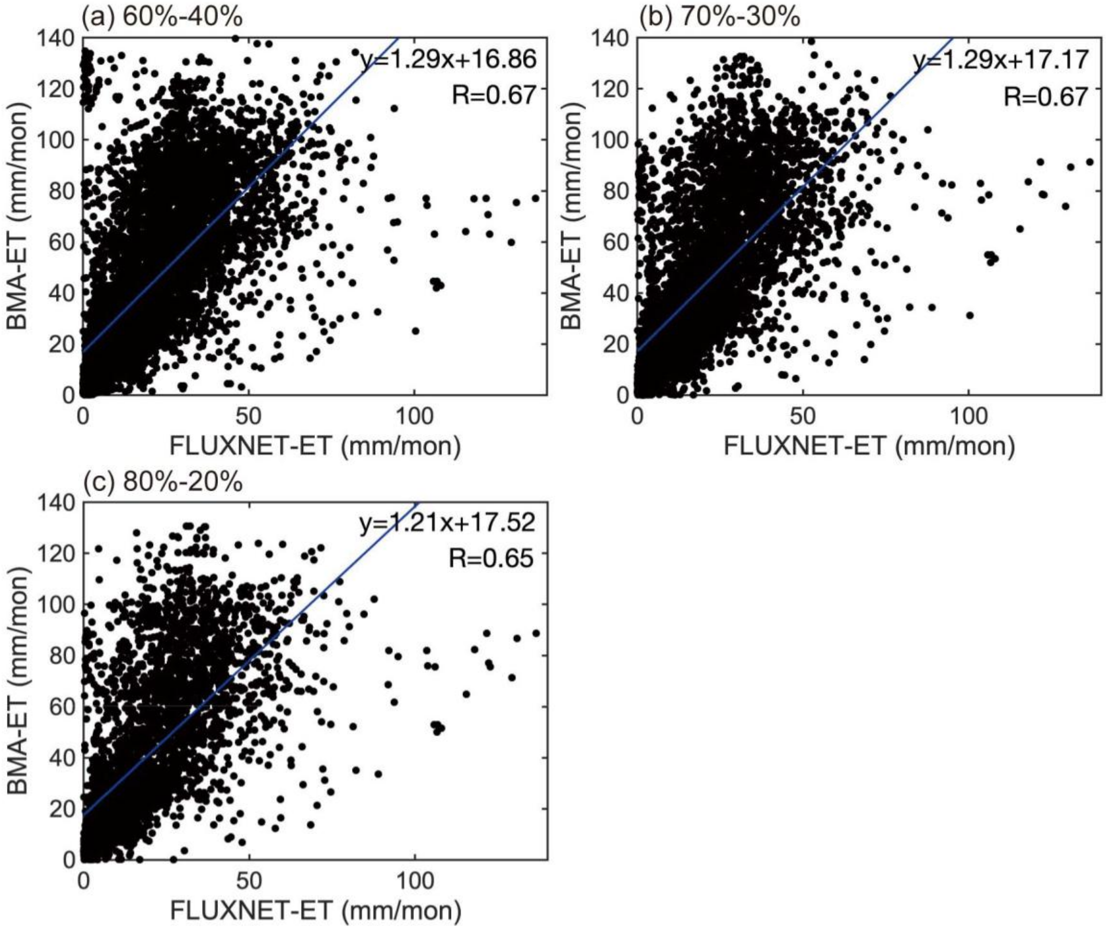

Fig. S29: Accuracy evaluation of BMA-ET. (a) 60% of data for training and 40% of data for validation, (b) 70% of data for training and 30% of data for validation, (c) 80% of data for training and 20% of data for validation.

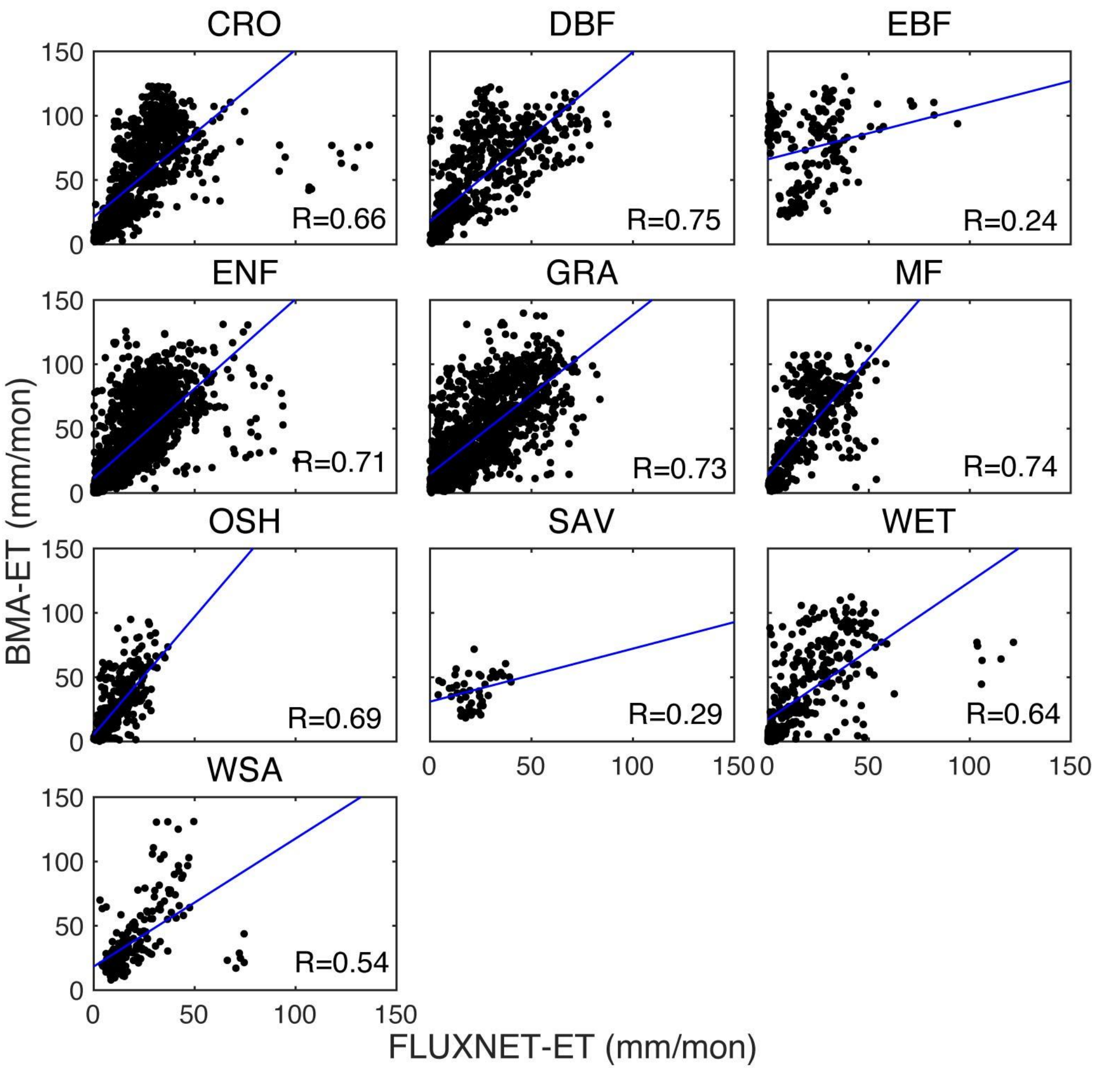

Fig. S30: Accuracy evaluation of BMA-ET over different vegetation types. 60% of data for training and 40% of data for validation.

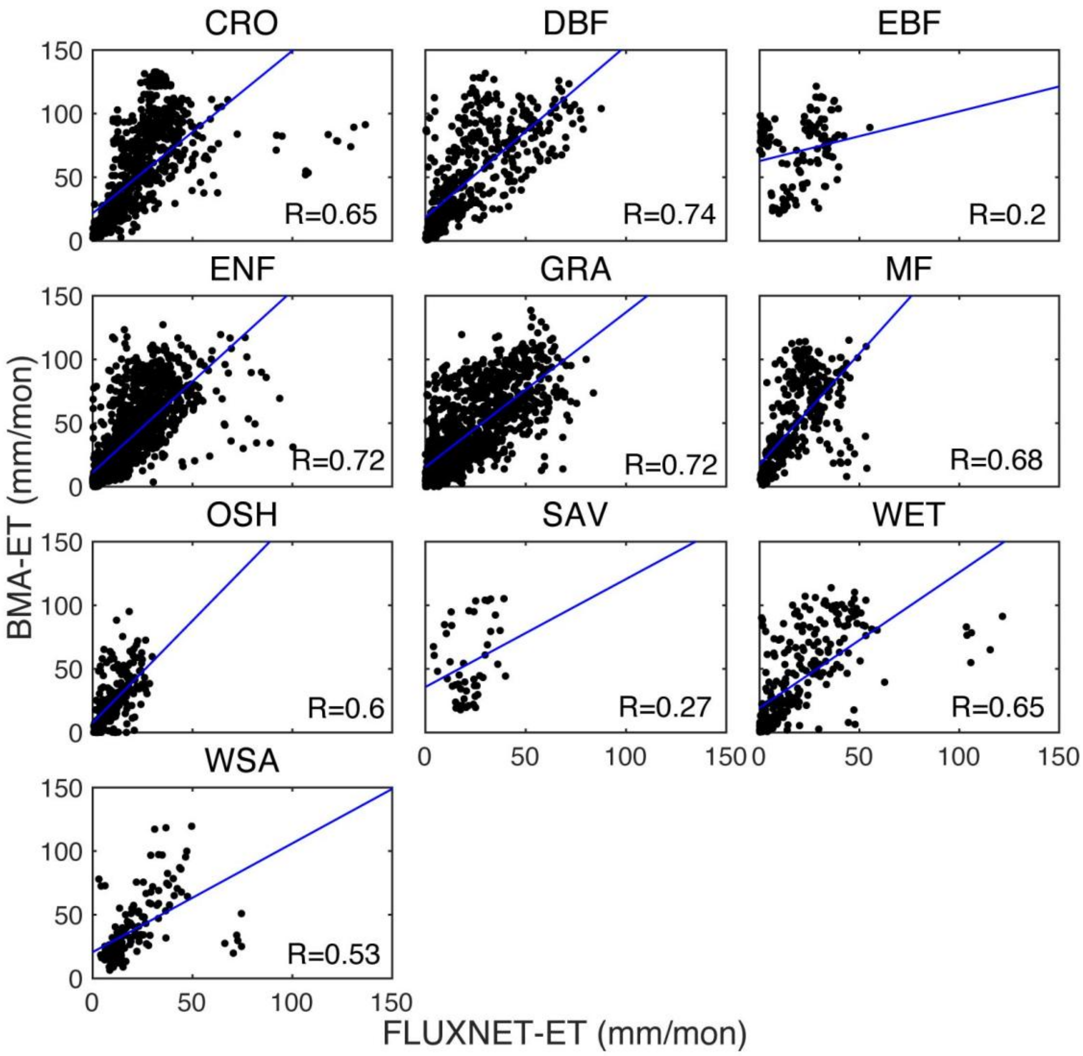

Fig. S31: Accuracy evaluation of BMA-ET over different vegetation types. 70% of data for training and 30% of data for validation.

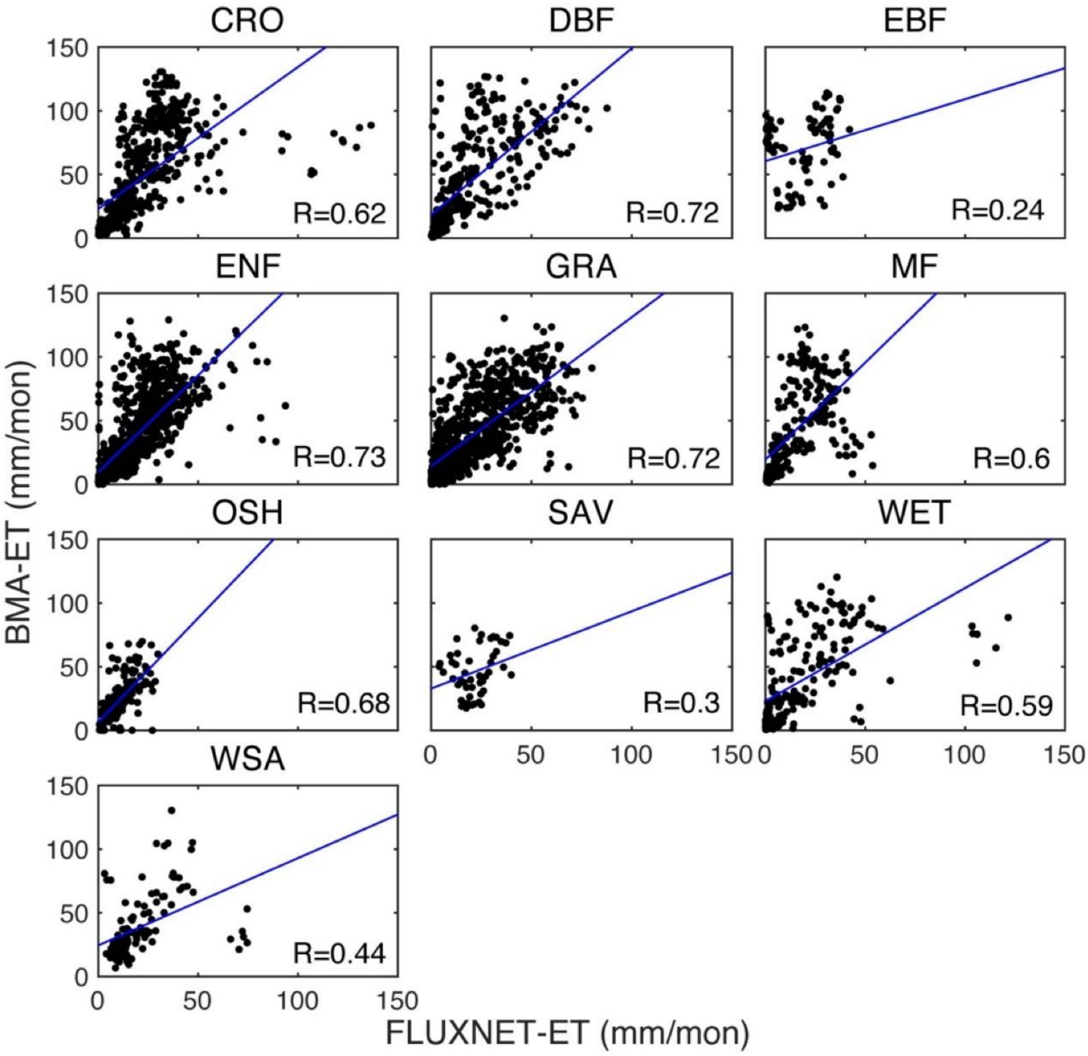

Fig. S32: Accuracy evaluation of BMA-ET over different vegetation types. 80% of data for training and 20% of data for validation.

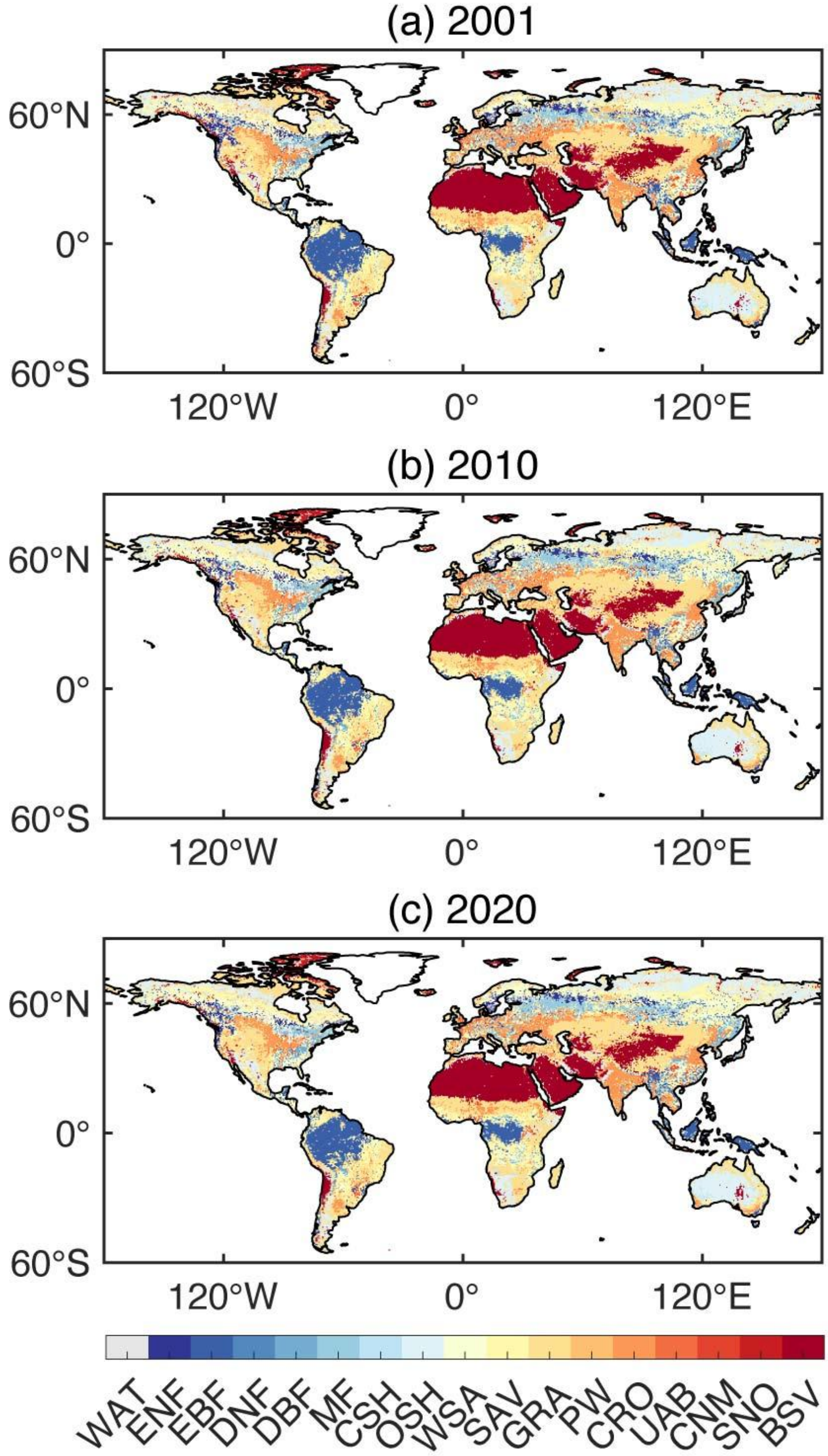

Fig. S33: Spatial distribution of land cover changes in three periods (2001, 2010, 2020) based on MOD12Q1.

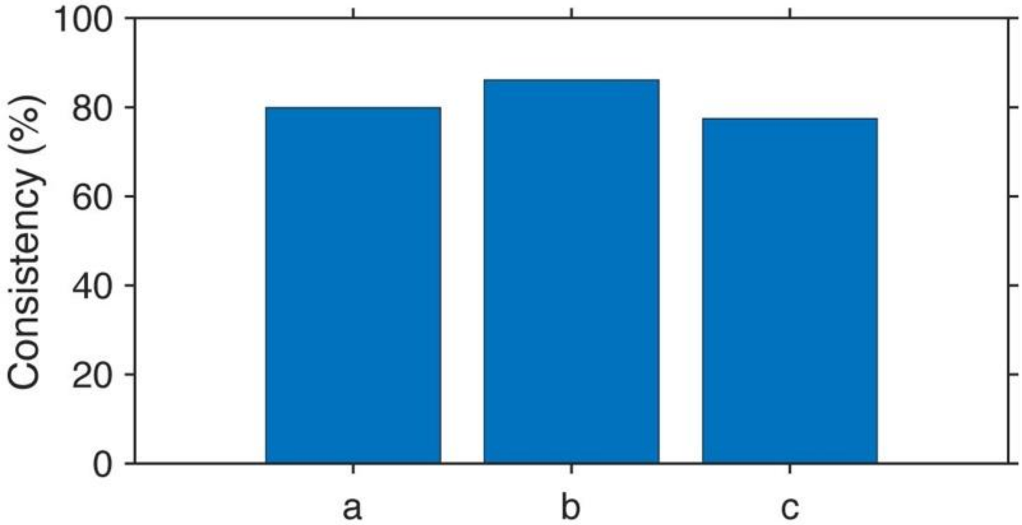

Fig. S34: Consistency between MOD12Q1 land cover types across years. Subfigures a-c show the level of consistency between land cover types for 2001 and 2010, 2010 and 2020, and 2001 and 2020, respectively. The level of consistency is characterized by the ratio of the number of grid points with consistent vegetation types to the total number of grid points on land.

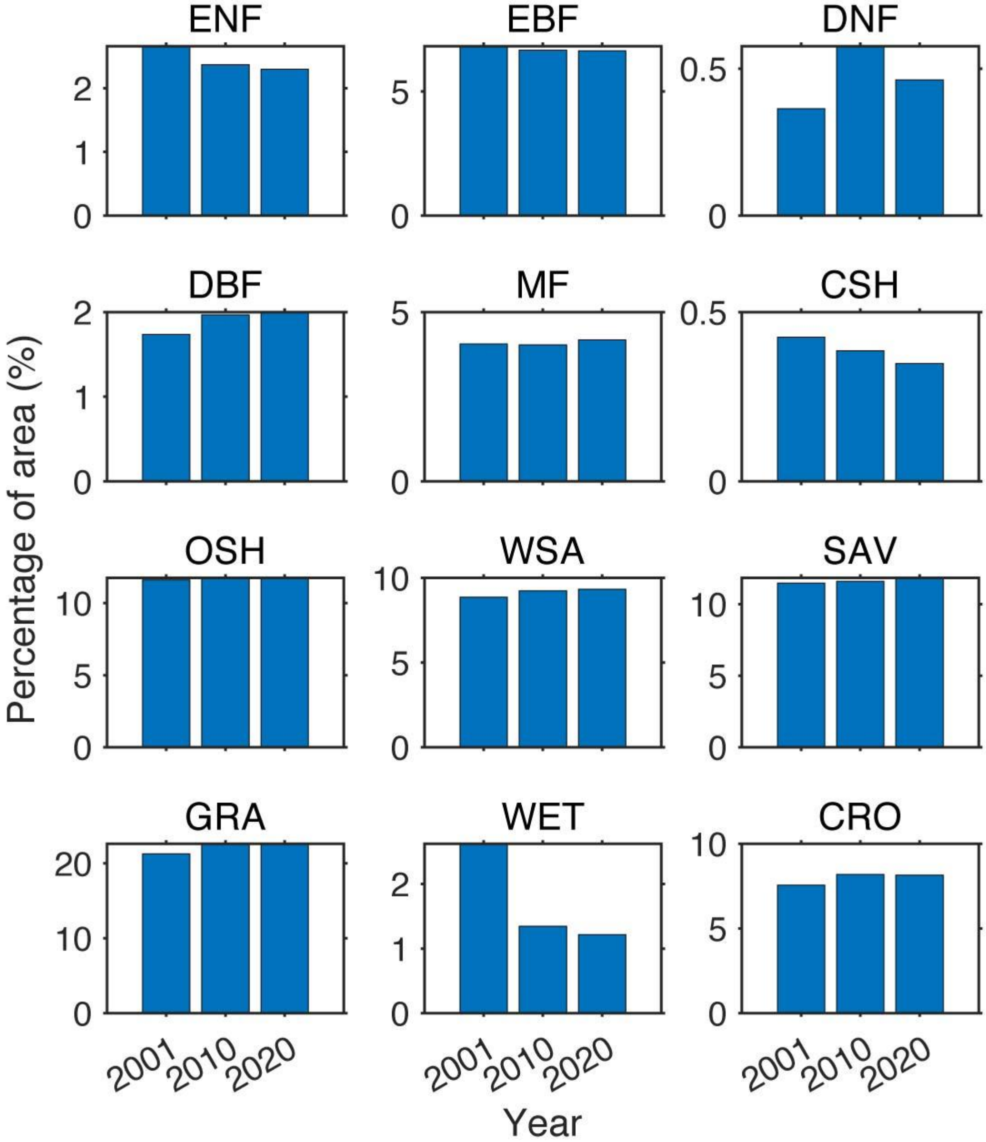

Fig. S35: Percentage of global land area covered by 12 vegetation types based on MOD12Q1. The bars in each subfigure represent the proportion of vegetation types in 2001, 2010 and 2020, respectively.

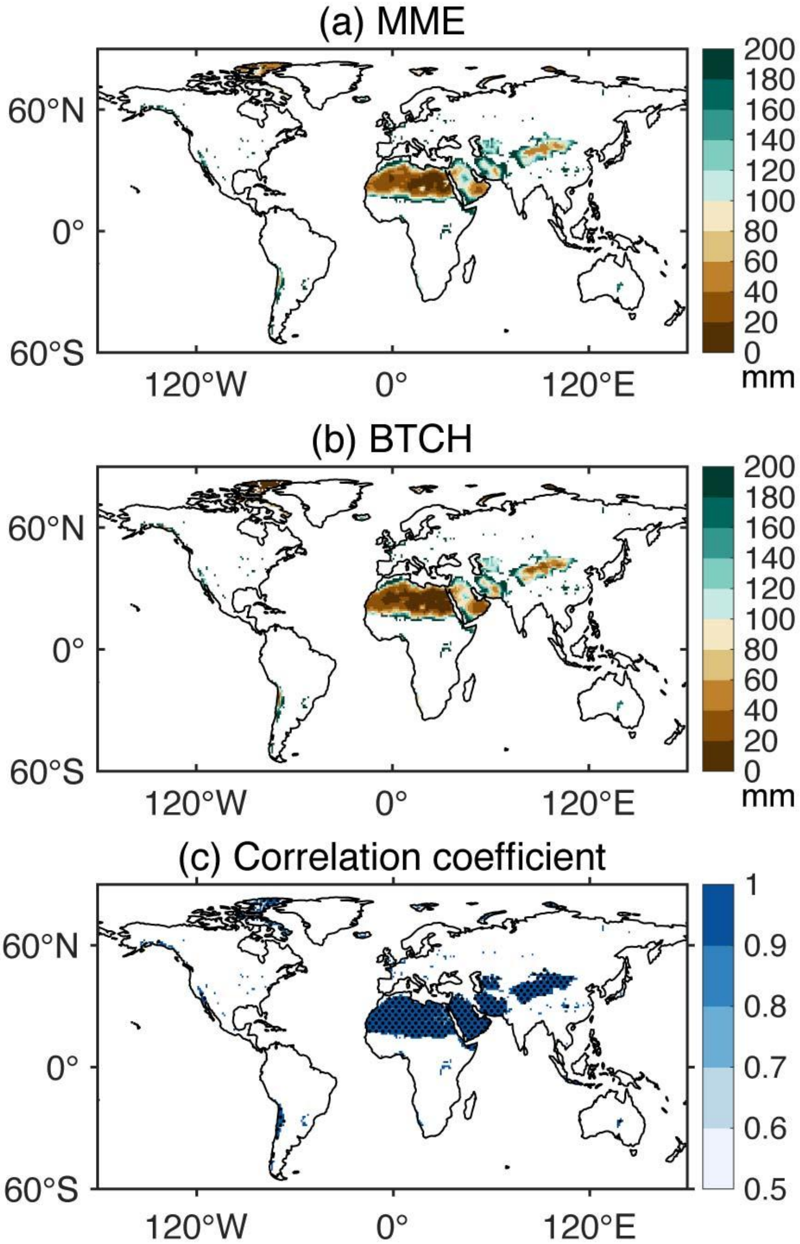

Fig. S36. Spatial distribution of multi-year average ET during 1980–2020 in the uncovered areas of 10 vegetation types. (a) the spatial distribution of ET based on the equal weight method, (b) the spatial distribution of ET based on the BTCH, (c) the correlation coefficient of ET between two methods, with the black dots representing that the ET of the grid point passed the significance test (*p*<0.05).

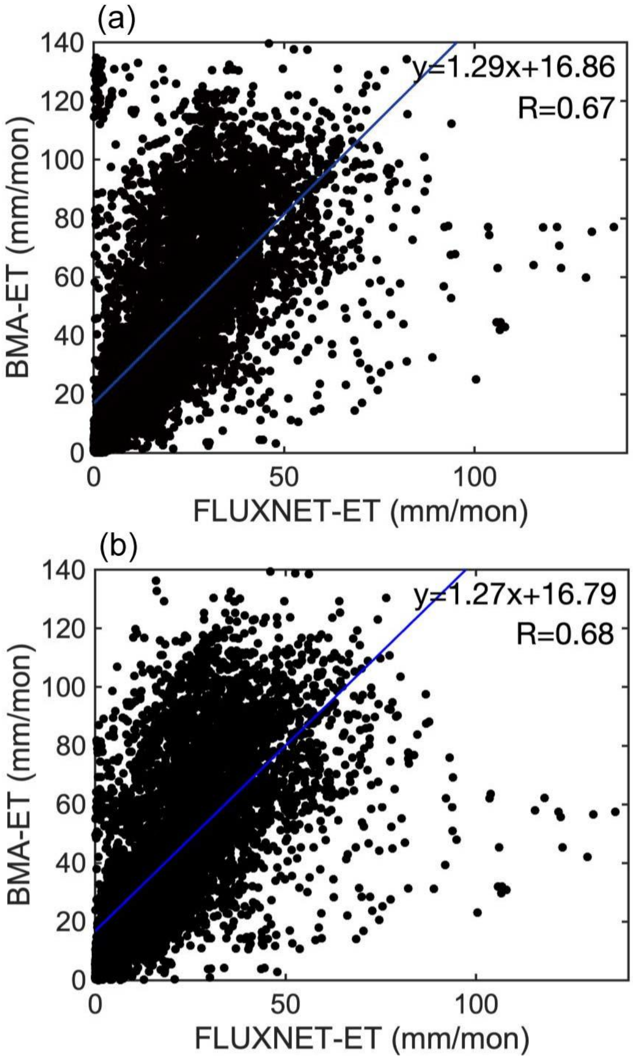

Fig. S37. Accuracy evaluation of BMA-ET using FLUXNET2015. 60% of data for training and 40% of data for validation. (a) BMA-ET fused with 30 sets of ET dataset, (b) BMA-ET fused with 24 sets of ET dataset.

Table S1. Data download links for evapotranspiration datasets.

ID	Name	Data download links
1	PML	https://doi.org/10.4225/08/5719A5C48DB85
2	GLEAM 3.6a	https://www.gleam.eu/#downloads
3	GLASS	http://www.glass.umd.edu/
4	PLSH	http://files.ntsg.umt.edu/data/ET_global_monthly/Global_8kmResolution/
5	FLUXCOM-CRUNCEP_v8	https://www.bgc-jena.mpg.de/geodb/projects/Data.php
6	FLUXCOM-GSWP3	https://www.bgc-jena.mpg.de/geodb/projects/Data.php
7	FLUXCOM-WFDEI	https://www.bgc-jena.mpg.de/geodb/projects/Data.php
8	MTE	https://www.bgc-jena.mpg.de/geodb/projects/DataDnld.php
9	ERA5-Land	https://cds.climate.copernicus.eu/datasets/reanalysis-era5-land-monthly-means?tab=download
10	MERRA-Land	https://gmao.gsfc.nasa.gov/reanalysis/MERRA-Land/data/
11	GLDAS CLSM 2.0	https://disc.gsfc.nasa.gov/datasets?keywords=GLDAS&page=1&source=Models%20Catchment-LSM
12	GLDAS NOAH 2.1	https://disc.gsfc.nasa.gov/datasets?keywords=GLDAS&page=1&source=Models%20Noah-LSM
13	GLDAS VIC	https://disc.gsfc.nasa.gov/datasets?keywords=GLDAS&page=1&source=Models%20VIC-LSM
14	CABLE-POP	——
15	CLASSIC	——
16	CLM5.0	——
17	DLEM	——

18	E3SM	——
19	EDv3	——
20	IBIS	——
21	ISBA-CTRIP	——
22	JSBACH	——
23	LPJ-GUESS	——
24	LPJmL	——
25	LPX-Bern	——
26	OCN	——
27	ORCHIDEE	——
28	SDGVM	——
29	VISIT	——
30	YIBs	——

Note: The TRENDY model simulations can be obtained by contacting Stephen Sitch (s.a.sitch@exeter.ac.uk) and Pierre Friedlingstein (p.friedlingstein@exeter.ac.uk).

Table S2. Vegetation types to which ET from FLUXNET (174) belong and the number of sites corresponding to each vegetation type.

ID	Name	Abbreviation	Number of sites
1	Croplands	CRO	16
2	Closed shrublands	CSH	2
3	Deciduous broadleaf forests	DBF	22
4	Deciduous needleleaf forests	DNF	1
5	Evergreen broadleaf forests	EBF	14
6	Evergreen needleleaf forests	ENF	42
7	Grasslands	GRA	33
8	Mixed forests	MF	9
9	Open shrublands	OSH	10
10	Savannas	SAV	3
11	Wetlands	WET	16
12	Woody savannas	WSA	6

Table S3. Vegetation types and time ranges for the 174 ET from FLUXNET2015 used in this study.

ID	Name	Latitude	Longitude	IGBP	Start year	End year
1	AR-SLu	−33.4648	−66.4598	MF	2009	2011
2	AR-Vir	−28.2395	−56.1886	ENF	2009	2012
3	AT-Neu	47.1167	11.3175	GRA	2002	2012
4	AU-ASM	−22.283	133.249	SAV	2010	2014
5	AU-Ade	−13.0769	131.1178	WSA	2007	2009
6	AU-Cpr	−34.0021	140.5891	SAV	2010	2014
7	AU-Cum	−33.6152	150.7236	EBF	2012	2014
8	AU-DaP	−14.0633	131.3181	GRA	2007	2013
9	AU-Emr	−23.8587	148.4746	GRA	2011	2013
10	AU-Fog	−12.5452	131.3072	WET	2006	2008
11	AU-Gin	−31.3764	115.7138	WSA	2011	2014
12	AU-How	−12.4943	131.1523	WSA	2001	2014
13	AU-RDF	−14.5636	132.4776	WSA	2011	2013
14	AU-Rig	−36.6499	145.5759	GRA	2011	2014
15	AU-Stp	−17.1507	133.3502	GRA	2008	2014
16	AU-TTE	−22.287	133.64	GRA	2012	2014
17	AU-Tum	−35.6566	148.1517	EBF	2001	2014
18	AU-Wac	−37.4259	145.1878	EBF	2005	2008
19	AU-Whr	−36.6732	145.0294	EBF	2011	2014
20	AU-Wom	−37.4222	144.0944	EBF	2010	2014
21	AU-Ync	−34.9893	146.2907	GRA	2012	2014
22	BE-Bra	51.3076	4.5198	MF	1996	2014
23	BE-Lon	50.5516	4.7462	CRO	2004	2014
24	BE-Vie	50.3049	5.9981	MF	1996	2014
25	BR-Sa1	−2.8567	−54.9589	EBF	2002	2011
26	BR-Sa3	−3.018	−54.9714	EBF	2000	2004
27	CA-Gro	48.2167	−82.1556	MF	2003	2014
28	CA-Man	55.8796	−98.4808	ENF	1994	2008
29	CA-NS1	55.8792	−98.4839	ENF	2001	2005

30	CA-NS2	55.9058	−98.5247	ENF	2001	2005
31	CA-NS3	55.9117	−98.3822	ENF	2001	2005
32	CA-NS4	55.9144	−98.3806	ENF	2002	2005
33	CA-NS5	55.8631	−98.485	ENF	2001	2005
34	CA-NS6	55.9167	−98.9644	OSH	2001	2005
35	CA-NS7	56.6358	−99.9483	OSH	2002	2005
36	CA-Oas	53.6289	−106.1978	DBF	1996	2010
37	CA-Obs	53.9872	−105.1178	ENF	1997	2010
38	CA-Qfo	49.6925	−74.3421	ENF	2003	2010
39	CA-SF1	54.485	−105.8176	ENF	2003	2006
40	CA-SF2	54.2539	−105.8775	ENF	2001	2005
41	CA-SF3	54.0916	−106.0053	OSH	2001	2006
42	CA-TP1	42.6609	−80.5595	ENF	2002	2014
43	CA-TP2	42.7744	−80.4588	ENF	2002	2007
44	CA-TP3	42.7068	−80.3483	ENF	2002	2014
45	CA-TP4	42.7102	−80.3574	ENF	2002	2014
46	CA-TPD	42.6353	−80.5577	DBF	2012	2014
47	CG-Tch	−4.2892	11.6564	SAV	2006	2009
48	CH-Cha	47.2102	8.4104	GRA	2005	2014
49	CH-Dav	46.8153	9.8559	ENF	1997	2014
50	CH-Fru	47.1158	8.5378	GRA	2005	2014
51	CH-Lae	47.4783	8.3644	MF	2004	2014
52	CH-Oe1	47.2858	7.7319	GRA	2002	2008
53	CH-Oe2	47.2864	7.7337	CRO	2004	2014
54	CN-Cha	42.4025	128.0958	MF	2003	2005
55	CN-Cng	44.5934	123.5092	GRA	2007	2010
56	CN-Din	23.1733	112.5361	EBF	2003	2005
57	CN-Du2	42.0467	116.2836	GRA	2006	2008
58	CN-Ha2	37.6086	101.3269	WET	2003	2005
59	CN-HaM	37.37	101.18	GRA	2002	2004
60	CN-Qia	26.7414	115.0581	ENF	2003	2005
61	CN-Sw2	41.7902	111.8971	GRA	2010	2012
62	CZ-BK1	49.5021	18.5369	ENF	2004	2014

63	CZ-BK2	49.4944	18.5429	GRA	2004	2012
64	CZ-wet	49.0247	14.7704	WET	2006	2014
65	DE-Akm	53.8662	13.6834	WET	2009	2014
66	DE-Geb	51.0997	10.9146	CRO	2001	2014
67	DE-Gri	50.95	13.5126	GRA	2004	2014
68	DE-Hai	51.0792	10.4522	DBF	2000	2012
69	DE-Kli	50.8931	13.5224	CRO	2004	2014
70	DE-Lkb	49.0996	13.3047	ENF	2009	2013
71	DE-Lnf	51.3282	10.3678	DBF	2002	2012
72	DE-Obe	50.7867	13.7213	ENF	2008	2014
73	DE-RuR	50.6219	6.3041	GRA	2011	2014
74	DE-RuS	50.8659	6.4471	CRO	2011	2014
75	DE-Seh	50.8706	6.4497	CRO	2007	2010
76	DE-SfN	47.8064	11.3275	WET	2012	2014
77	DE-Spw	51.8922	14.0337	WET	2010	2014
78	DE-Tha	50.9626	13.5651	ENF	1996	2014
79	DK-Eng	55.6905	12.1918	GRA	2005	2008
80	DK-Sor	55.4859	11.6446	DBF	1996	2014
81	ES-Amo	36.8336	−2.2523	OSH	2007	2012
82	ES-LJu	36.9266	−2.7521	OSH	2004	2013
83	ES-LgS	37.0979	−2.9658	OSH	2007	2009
84	FI-Hyy	61.8474	24.2948	ENF	1996	2014
85	FI-Jok	60.8986	23.5134	CRO	2000	2003
86	FI-Let	60.6418	23.9595	ENF	2009	2012
87	FI-Lom	67.9972	24.2092	WET	2007	2009
88	FI-Sod	67.3624	26.6386	ENF	2001	2014
89	FR-Fon	48.4764	2.7801	DBF	2005	2014
90	FR-Gri	48.8442	1.9519	CRO	2004	2014
91	FR-LBr	44.7171	−0.7693	ENF	1996	2008
92	FR-Pue	43.7413	3.5957	EBF	2000	2014
93	GF-Guy	5.2788	−52.9249	EBF	2004	2014
94	GH-Ank	5.2685	−2.6942	EBF	2011	2014
95	GL-NuF	64.1308	−51.3861	WET	2008	2014

96	IT-BCi	40.5237	14.9574	CRO	2004	2014
97	IT-CA1	42.3804	12.0266	DBF	2011	2014
98	IT-CA2	42.3772	12.026	CRO	2011	2014
99	IT-CA3	42.38	12.0222	DBF	2011	2014
100	IT-Col	41.8494	13.5881	DBF	1996	2014
101	IT-Cp2	41.7043	12.3573	EBF	2012	2014
102	IT-Cpz	41.7052	12.3761	EBF	1997	2009
103	IT-La2	45.9542	11.2853	ENF	2000	2002
104	IT-Lav	45.9562	11.2813	ENF	2003	2014
105	IT-MBo	46.0147	11.0458	GRA	2003	2013
106	IT-Noe	40.6062	8.1517	CSH	2004	2014
107	IT-PT1	45.2009	9.061	DBF	2002	2004
108	IT-Ren	46.5869	11.4337	ENF	1998	2013
109	IT-Ro1	42.4081	11.93	DBF	2000	2008
110	IT-Ro2	42.3903	11.9209	DBF	2002	2012
111	IT-SRo	43.7279	10.2844	ENF	1999	2012
112	IT-Tor	45.8444	7.5781	GRA	2008	2014
113	JP-MBF	44.3869	142.3186	DBF	2003	2005
114	JP-SMF	35.2617	137.0788	MF	2002	2006
115	MY-PSO	2.973	102.3062	EBF	2003	2009
116	NL-Hor	52.2403	5.0713	GRA	2004	2011
117	NL-Loo	52.1666	5.7436	ENF	1996	2014
118	PA-SPn	9.3181	−79.6346	DBF	2007	2009
119	PA-SPs	9.3138	−79.6314	GRA	2007	2009
120	RU-Che	68.613	161.3414	WET	2002	2005
121	RU-Cok	70.8291	147.4943	OSH	2003	2014
122	RU-Fyo	56.4615	32.9221	ENF	1998	2014
123	RU-Ha1	54.7252	90.0022	GRA	2002	2004
124	RU-Sam	72.3738	126.4958	GRA	2002	2014
125	RU-SkP	62.255	129.168	DNF	2012	2014
126	RU-Tks	71.5943	128.8878	GRA	2010	2014
127	SE-St1	68.3541	19.0503	WET	2012	2014
128	US-AR1	36.4267	−99.42	GRA	2009	2012

129	US-AR2	36.6358	−99.5975	GRA	2009	2012
130	US-ARM	36.6058	−97.4888	CRO	2003	2012
131	US-Atq	70.4696	−157.4089	WET	2003	2008
132	US-Blo	38.8953	−120.6328	ENF	1997	2007
133	US-CRT	41.6285	−83.3471	CRO	2011	2013
134	US-Cop	38.09	−109.39	GRA	2001	2007
135	US-GBT	41.3658	−106.2397	ENF	1999	2006
136	US-GLE	41.3665	−106.2399	ENF	2004	2014
137	US-Goo	34.2547	−89.8735	GRA	2002	2006
138	US-Ha1	42.5378	−72.1715	DBF	1991	2012
139	US-IB2	41.8406	−88.241	GRA	2004	2011
140	US-Ivo	68.4865	−155.7503	WET	2004	2007
141	US-KS2	28.6086	−80.6715	CSH	2003	2006
142	US-Los	46.0827	−89.9792	WET	2000	2014
143	US-MMS	39.3232	−86.4131	DBF	1999	2014
144	US-Me2	44.4523	−121.5574	ENF	2002	2014
145	US-Me3	44.3154	−121.6078	ENF	2004	2009
146	US-Me4	44.4992	−121.6224	ENF	1996	2000
147	US-Me5	44.4372	−121.5668	ENF	2000	2002
148	US-Me6	44.3233	−121.6078	ENF	2010	2014
149	US-Myb	38.0499	−121.765	WET	2010	2014
150	US-NR1	40.0329	−105.5464	ENF	1998	2014
151	US-Ne1	41.1651	−96.4766	CRO	2001	2013
152	US-Ne2	41.1649	−96.4701	CRO	2001	2013
153	US-Ne3	41.1797	−96.4397	CRO	2001	2013
154	US-Oho	41.5545	−83.8438	DBF	2004	2013
155	US-PFa	45.9459	−90.2723	MF	1995	2014
156	US-Prr	65.1237	−147.4876	ENF	2010	2014
157	US-SRC	31.9083	−110.8395	OSH	2008	2014
158	US-SRG	31.7894	−110.8277	GRA	2008	2014
159	US-SRM	31.8214	−110.8661	WSA	2004	2014
160	US-Sta	41.3966	−106.8024	OSH	2005	2009
161	US-Syv	46.242	−89.3477	MF	2001	2014

162	US-Ton	38.4309	−120.966	WSA	2001	2014
163	US-Tw1	38.1074	−121.6469	WET	2012	2014
164	US-Twt	38.1087	−121.6531	CRO	2009	2014
165	US-UMB	45.5598	−84.7138	DBF	2000	2014
166	US-UMd	45.5625	−84.6975	DBF	2007	2014
167	US-Var	38.4133	−120.9508	GRA	2000	2014
168	US-WCr	45.8059	−90.0799	DBF	1999	2014
169	US-WPT	41.4646	−82.9962	WET	2011	2013
170	US-Whs	31.7438	−110.0522	OSH	2007	2014
171	US-Wi3	46.6347	−91.0987	DBF	2002	2004
172	US-Wi4	46.7393	−91.1663	ENF	2002	2005
173	US-Wkg	31.7365	−109.9419	GRA	2004	2014
174	ZM-Mon	−15.4391	23.2525	DBF	2000	2009

Table S4. The variable information from ET from FLUXNET used in this study.

ID	Variable name	Full name of variable
1	P_F	Precipitation
2	LE_F_MDS	Latent heat flux
3	H_F_MDS	Sensible heat flux
4	G_F_MDS	Soil heat flux
5	RH	Relative humidity
6	NETRAD	Net radiation

Table S5. Basic information of AmeriFlux.

Site ID	Site Name	Vegetation Abbreviation (IGBP)	Lon	Lat	Data Start	Data End
1	AR-CCg	GRA	-61.1855°E	-35.9244°N	2018	2024
2	AR-TF1	WET	-66.7335°E	-54.9733°N	2016	2018
3	BR-CST	DNF	-38.3842°E	-7.9682°N	2014	2015
4	BR-Npw	WSA	-56.4120°E	-16.4980°N	2013	2017
5	CA-ARB	WET	-83.9452°E	52.6950°N	2011	2015
6	CA-ARF	WET	-83.9550°E	52.7008°N	2011	2015
7	CA-BOU	WET	-63.2064°E	50.5244°N	2018	2020
8	CA-Ca1	ENF	-125.3336°E	49.8673°N	1996	2010
9	CA-Ca2	ENF	-125.2909°E	49.8705°N	1999	2010
10	CA-Cbo	DBF	-79.9341°E	44.3184°N	1994	2020
11	CA-CF1	WET	-93.8300°E	58.6658°N	2007	2008
12	CA-DB2	WET	-122.9951°E	49.119°0N	2019	2020
13	CA-DBB	WET	-122.9849°E	49.1293°N	2014	2020
14	CA-ER1	CRO	-80.4123°E	43.6405°N	2015	2021
15	CA-HPC	ENF	-133.5188°E	68.3203°N	2018	2018
16	CA-LP1	ENF	-122.8414°E	55.1119°N	2007	2022
17	CA-MA1	CRO	-97.8762°E	50.1645°N	2009	2011
18	CA-MA2	CRO	-97.8762°E	50.1710°N	2009	2011
19	CA-MA3	GRA	-97.8686°E	50.1774°N	2009	2011
20	CA-Qc2	MF	-74.5711°E	49.7598°N	2007	2010
21	CA-SCB	WET	-121.2984°E	61.3089°N	2014	2019
22	CA-SCC	ENF	-121.2992°E	61.3079°N	2013	2024
23	CL-SDF	EBF	-73.6760°E	-41.8830°N	2014	2022
24	MX-Tes	DBF	-109.2977°E	27.8446°N	2004	2008
25	PE-QFR	WET	-73.3190°E	-3.8344°N	2018	2022

26	US-A32	GRA	-97.8198°E	36.8193°N	2015	2017
27	US-A74	CRO	-97.5489°E	36.8085°N	2015	2017
28	US-Akn	MF	-81.5653°E	33.3825°N	2011	2022
29	US-ALQ	WET	-89.6067°E	46.0308°N	2015	2024
30	US-ASH	DBF	-120.2010°E	36.1697°N	2016	2017
31	US-ASM	DBF	-120.2026°E	36.1777°N	2016	2017
32	US-Bar	DBF	-71.2881°E	44.0646°N	2004	2024
33	US-Bi1	CRO	-121.4993°E	38.0992°N	2016	2024
34	US-Bi2	CRO	-121.5351°E	38.1091°N	2017	2024
35	US-BRG	GRA	-86.5406°E	39.2167°N	2016	2020
36	US-BZB	WET	-148.3208°E	64.6955°N	2011	2024
37	US-BZF	WET	-148.3121°E	64.7013°N	2011	2024
38	US-BZo	WET	-148.3300°E	64.6936°N	2018	2024
39	US-BZS	ENF	-148.3235°E	64.6963°N	2010	2024
40	US-CdM	WSA	-109.7471°E	37.5241°N	2019	2023
41	US-CF1	CRO	-117.0821°E	46.7815°N	2017	2021
42	US-CF2	CRO	-117.0908°E	46.7840°N	2017	2021
43	US-CF3	CRO	-117.1261°E	46.7551°N	2017	2021
44	US-CF4	CRO	-117.1285°E	46.7518°N	2017	2021
45	US-CGG	GRA	-121.9761°E	37.9380°N	2019	2022
46	US-CS1	CRO	-89.5379°E	44.1031°N	2018	2019
47	US-CS2	ENF	-89.5002°E	44.1467°N	2018	2022
48	US-CS3	CRO	-89.5727°E	44.1394°N	2019	2020
49	US-CS4	CRO	-89.5475°E	44.1597°N	2020	2021
50	US-Cst	ENF	-91.9204°E	33.0442°N	2013	2017
51	US-DFC	CRO	-89.7117°E	43.3448°N	2018	2024
52	US-EDN	WET	-122.1140°E	37.6156°N	2018	2021
53	US-EML	OSH	-149.2536°E	63.8784°N	2008	2020
54	US-Fcr	OSH	-148.9348°E	65.3968°N	2011	2014
55	US-Fmf	ENF	-111.7273°E	35.1426°N	2005	2010
56	US-Fuf	ENF	-111.7620°E	35.0890°N	2005	2010
57	US-Fwf	GRA	-111.7718°E	35.4454°N	2005	2010
58	US-HB1	WET	-79.1957°E	33.3455°N	2019	2022

59	US-HB2	ENF	-79.244°E	33.3242°N	2019	2019
60	US-HB3	ENF	-79.2322°E	33.3482°N	2019	2022
61	US-Hn2	GRA	-119.4641°E	46.6889°N	2015	2018
62	US-Hn3	OSH	-119.4614°E	46.6878°N	2017	2018
63	US-Ho1	ENF	-68.7402°E	45.2041°N	1996	2024
64	US-Ho2	ENF	-68.7470°E	45.2091°N	1999	2024
65	US-HWB	CVM	-77.8488°E	40.8608°N	2015	2018
66	US-ICh	OSH	-149.2958°E	68.6068°N	2007	2024
67	US-ICs	WET	-149.3110°E	68.6058°N	2007	2024
68	US-ICt	OSH	-149.3041°E	68.6063°N	2007	2024
69	US-Jo1	OSH	-106.6350°E	32.5820°N	2010	2022
70	US-Jo2	OSH	-106.6032°E	32.5849°N	2010	2020
71	US-KFS	GRA	-95.1907°E	39.0561°N	2007	2019
72	US-KLS	GRA	-97.5684°E	38.7745°N	2012	2019
73	US-Kon	GRA	-96.5603°E	39.0824°N	2004	2019
74	US-KS3	WET	-80.7427°E	28.7084°N	2018	2019
75	US-LS2	SAV	-110.1344°E	31.5659°N	2002	2007
76	US-Mo1	CRO	-92.1167°E	39.2298°N	2015	2024
77	US-Mo2	GRA	-91.9945°E	38.9488°N	2018	2024
78	US-Mo3	CRO	-92.1493°E	39.2322°N	2016	2023
79	US-MOz	DBF	-92.2000°E	38.7441°N	2004	2021
80	US-Mpj	WSA	-106.2377°E	34.4385°N	2008	2024
81	US-NC1	ENF	-76.7119°E	35.8118°N	2005	2012
82	US-NC3	ENF	-76.6560°E	35.7990°N	2013	2021
83	US-NC4	WET	-75.9038°E	35.7879°N	2009	2025
84	US-OWC	WET	-82.5125°E	41.3795°N	2015	2024
85	US-PFb	ENF	-90.3232°E	45.9720°N	2019	2019
86	US-PFc	DBF	-90.3088°E	45.9677°N	2019	2019
87	US-PFd	WET	-90.3010°E	45.9689°N	2019	2019
88	US-PFk	DBF	-90.3425°E	45.9149°N	2019	2019
89	US-PFL	DBF	-90.3177°E	45.9409°N	2019	2019

90	US-PFm	DBF	-90.3099°E	45.9207°N	2019	2019
91	US-PFn	DBF	-90.2823°E	45.9392°N	2019	2019
92	US-PFp	DBF	-90.2641°E	45.9365°N	2019	2019
93	US-PFq	DBF	-90.2475°E	45.9271°N	2019	2019
94	US-PFt	ENF	-90.2288°E	45.9197°N	2019	2019
95	US-Pnp	WAT	-89.4158°E	43.0896°N	2016	2022
96	US-PSH	DBF	-119.9247°E	36.2347°N	2016	2017
97	US-PSL	DBF	-120.1397°E	36.8276°N	2016	2017
98	US-Rls	CSH	-116.7356°E	43.1439°N	2014	2023
99	US-Rms	CSH	-116.7486°E	43.0645°N	2014	2023
100	US-Ro1	CRO	-93.0898°E	44.7143°N	2004	2016
101	US-Ro2	CRO	-93.0888°E	44.7288°N	2008	2016
102	US-Ro3	CRO	-93.0893°E	44.7217°N	2004	2007
103	US-Ro4	GRA	-93.0723°E	44.6781°N	2014	2024
104	US-Ro5	CRO	-93.0576°E	44.6910°N	2017	2024
105	US-Ro6	CRO	-93.0578°E	44.6946°N	2017	2024
106	US-Rpf	DBF	-147.429°E	65.1198°N	2008	2024
107	US-Rwe	CSH	-116.7591°E	43.0653°N	2003	2007
108	US-Rwf	CSH	-116.7231°E	43.1207°N	2014	2023
109	US-Rws	OSH	-116.7132°E	43.1675°N	2014	2023
110	US-Seg	GRA	-106.7020°E	34.3623°N	2007	2024
111	US-Ses	OSH	-106.7442°E	34.3349°N	2007	2024
112	US-Sne	GRA	-121.7547°E	38.0369°N	2016	2020
113	US-Snf	GRA	-121.7272°E	38.0402°N	2018	2020
114	US-SP1	ENF	-82.2188°E	29.7381°N	2000	2020
115	US-Srr	WET	-122.0264°E	38.2006°N	2014	2017
116	US-SRS	WSA	-110.8508°E	31.8173°N	2011	2018
117	US-SSH	DBF	-77.9041°E	40.6658°N	2016	2021
118	US-StJ	WET	-75.4372°E	39.0882°N	2014	2017
119	US-Tw5	WET	-121.6426°E	38.1072°N	2018	2020
120	US-UC1	CVM	-78.0056°E	40.7536°N	2019	2024
121	US-UC2	CVM	-77.9998°E	40.7559°N	2019	2024
122	US-UM3	WAT	-84.6707°E	45.5686°N	2013	2014

123	US-Vcm	ENF	-106.5321°E	35.8884°N	2007	2023
124	US-Vcp	ENF	-106.5967°E	35.8642°N	2007	2024
125	US-Wjs	SAV	-105.8615°E	34.4255°N	2007	2024
126	US-WPT	WET	-82.9962°E	41.4646°N	2011	2013
127	US-xAB	ENF	-122.3303°E	45.7624°N	2017	2023
128	US-xAE	GRA	-99.0588°E	35.4106°N	2017	2023
129	US-xBA	WET	-156.6194°E	71.2824°N	2017	2023
130	US-xBL	DBF	-78.0716°E	39.0603°N	2017	2023
131	US-xBN	ENF	-147.5026°E	65.1540°N	2017	2023
132	US-xBR	DBF	-71.2873°E	44.0639°N	2017	2023
133	US-xCL	GRA	-97.5700°E	33.4012°N	2017	2023
134	US-xCP	GRA	-104.7456°E	40.8155°N	2016	2023
135	US-xDC	GRA	-99.1066°E	47.1617°N	2017	2023
136	US-xDJ	ENF	-145.7514°E	63.8811°N	2017	2023
137	US-xDL	MF	-87.8039°E	32.5417°N	2017	2023
138	US-xDS	CVM	-81.4362°E	28.1250°N	2017	2023
139	US-xGR	DBF	-83.5019°E	35.6890°N	2017	2023
140	US-xHA	DBF	-72.1727°E	42.5369°N	2017	2023
141	US-xHE	OSH	-149.2133°E	63.8757°N	2017	2023
142	US-xJE	ENF	-84.4686°E	31.1948°N	2017	2023
143	US-xJR	OSH	-106.8425°E	32.5907°N	2017	2023
144	US-xKA	GRA	-96.6129°E	39.1104°N	2017	2023
145	US-xKZ	GRA	-96.5631°E	39.1008°N	2017	2023
146	US-xMB	OSH	-109.3883°E	38.2483°N	2017	2023
147	US-xML	DBF	-80.5248°E	37.3783°N	2017	2023
148	US-xNG	GRA	-100.9154°E	46.7697°N	2017	2023
149	US-xNQ	OSH	-112.4524°E	40.1776°N	2017	2023
150	US-xRM	ENF	-105.5459°E	40.2759°N	2017	2023
151	US-xSB	ENF	-81.9934°E	29.6893°N	2017	2023
152	US-xSC	DBF	-78.1395°E	38.8929°N	2016	2023
153	US-xSE	DBF	-76.5600°E	38.8901°N	2017	2023
154	US-xSJ	SAV	-119.7323°E	37.1088°N	2018	2023
155	US-xSL	CRO	-103.0293°E	40.4619°N	2017	2023

156	US-xSR	OSH	-110.8355°E	31.9107°N	2017	2023
157	US-xST	DBF	-89.5864°E	45.5089°N	2017	2023
158	US-xTA	ENF	-87.3933°E	32.9505°N	2017	2023
159	US-xTL	WET	-149.3705°E	68.6611°N	2017	2023
160	US-xTR	DBF	-89.5857°E	45.4937°N	2017	2023
161	US-xUK	DBF	-95.1921°E	39.0404°N	2017	2023
162	US-xUN	MF	-89.5373°E	46.2339°N	2017	2023
163	US-xWD	GRA	-99.2414°E	47.1282°N	2017	2023
164	US-xYE	ENF	-110.5391°E	44.9535°N	2018	2023
165	US-YK2	WET	-163.259°E	61.2548°N	2019	2024

Table S6. Basic information of ChinaFlux.

Site ID	Site Name	Lon	Lat	Data Start	Data End
1	Xishuangbanna	101°12′E	21°57′N	2003	2010
2	Dinghushan	112°34′E	23°10′N	2003	2010
3	Haibei	101°20′E	37°40′N	2003	2010
4	Qianyanzhou	115°03′E	26°44′N	2003	2010
5	Yucheng	36°57′E	116°36′N	2003	2010
6	Changbaishan	128°05′E	42°24′N	2003	2010
7	Dangxiong	91°05′E	30°51′N	2004	2010
8	Inner Mongolia	117°10′E	44°30′N	2004	2010

Table S7. Basic information of ICOS.

Site ID	Site Name	Lon	Lat	Data Start	Data End
1	BE-Maa	5.6315°E	50.9798°N	2020	2022
2	CD-Ygb	24.5024°E	0.8144°N	2020	2022
3	DE-BeR	13.3158°E	52.4572°N	2018	2022
4	DE-Har	7.5981°E	47.9330°N	2020	2022
5	DE-HoH	11.2217°E	52.0860°N	2019	2022
6	DE-Msr	11.4561°E	47.8091°N	2020	2022
7	DE-RuW	6.3309°E	50.5049°N	2012	2022
8	DK-Vng	9.1607°E	56.0374°N	2020	2022
9	ES-LMa	-5.7746°E	39.9403°N	2020	2022
10	FI-Ken	24.2430°E	67.9872°N	2020	2022
11	FI-Kmp	24.9611°E	60.2028°N	2018	2022
12	FI-Kvr	24.2804°E	61.8466°N	2018	2022
13	FI-Sii	24.1928°E	61.8326°N	2018	2022
14	FI-Var	29.6100°E	67.7549°N	2017	2022
15	FR-Aur	1.1061°E	43.5496°N	2019	2022
16	FR-Bil	-0.9560°E	44.4936°N	2019	2022
17	FR-EM2	3.0206°E	49.8721°N	2017	2022
18	FR-Lam	1.2378°E	43.4964°N	2020	2022
19	FR-Mej	-1.7963°E	48.1184°N	2019	2022
20	FR-Tou	1.3747°E	43.5728°N	2018	2022
21	GL-Dsk	-53.5141°E	69.2534°N	2020	2022
22	IT-BFt	10.7419°E	45.1977°N	2019	2022
23	IT-Lsn	12.7502°E	45.7404°N	2016	2022
24	IT-Niv	7.1394°E	45.4909°N	2019	2022
25	SE-Deg	19.5565°E	64.1820°N	2019	2022
26	SE-Htm	13.4189°E	56.0976°N	2018	2022
27	SE-Nor	17.4795°E	60.0865°N	2018	2022
28	SE-Svb	19.7745°E	64.2561°N	2019	2022

Table S8. Basin information.

ID	Basin name	Country	Station name	Station longitude	Station latitude	Starting and ending year
1	Amazon	Brazil	Obidos	−55.51	−1.95	1927–2018
2	Amur	Russia	Komsomolsk	137.00	50.53	1900–2006
3	Churchill	Canada	Churchill River	−94.62	58.12	1928–2013
4	Columbia	USA	The Dalles	−121.17	45.61	1900–2018
5	Congo	Congo	Kinshasa	15.30	−4.30	1903–2010
6	Danube	Romania	Ceatal Izma	28.73	45.22	1900–2010
7	Don	Russia	Razdorskaya	40.65	47.53	1881–2010
8	Fraser	Canada	Hope	−121.45	49.38	1912–2016
9	Huaihe	China	Bengbu	117.37	32.94	1915–2004
10	Kolyma	Russia	Kolymskoye	158.72	68.73	1927–2008
11	Lena	Russia	Kusur	127.39	70.68	1934–2011
12	MacKenzie	Canada	Arctic Red	−133.74	67.46	1943–2016
13	Mekong	Laos	Pakse	105.80	15.11	1923–2005
14	Mississippi	USA	Vicksburg	−90.91	32.31	1928–2018
15	Nelson	Canada	Upstream of Bladder	−97.92	54.77	1915–2016
16	Niger	Nigeria	Lokoja	6.77	7.80	1915–2012
17	Ob’	Russia	Salekhard	66.60	66.63	1930–2015
18	Orange	South Africa	Vioolsdrift	17.63	−28.78	1935–2018
19	Ottawa	Canada	Chats Falls	−76.23	45.47	1914–2018
20	Paraná	Argentina	Timbues	−60.71	−32.67	1905–2018
21	Parnaiba	Brazil	Porto Formo	−42.37	−3.46	1955–2018
22	Pechora	Russia	Oksino	52.18	67.63	1916–2014
23	Rhine	Netherlands	Lobith	6.11	51.85	1901–2017
24	Saõ Francisco	Brazil	Traipu	−36.99	−9.98	1926–2018

25	Severnaya Dvina	Russia	Ust Pinega	41.92	64.13	1900–2014
26	Saint Lawrence	Canada	Cornwall ON	−74.74	45.00	1900–2018
27	Tocantins	Brazil	Tucurui	−49.67	−3.76	1955–2018
28	Uruguay	Argentina	Concordia	−58.03	−31.40	1942–2018
29	Yangtze	China	Datong	117.62	30.77	1960–2016
30	Yellow River	China	Lijin	118.25	37.50	1960–2014
31	Yenisei	Russia	Igarka	86.48	67.43	1936–2015
32	Yukon	USA	Pilot Station	−162.88	61.93	1956–2018

Table S9. Clustering results of 30 ET datasets in different vegetation types. ET products with the same number were clustered under each vegetation type.

	Datasets	CRO	DBF	EBF	ENF	GRA	MF	OSH	SAV	WET	WSA
1	PML	3	4	4	1	3	2	8	4	5	3
2	GLEAM	2	4	4	4	4	3	7	8	5	8
3	GLASS	3	4	4	1	1	2	3	7	5	6
4	PLSH	3	4	4	4	6	2	4	5	5	2
5	FLUXCOM-CRUNCEP_v8	3	4	4	1	3	2	7	9	5	3
6	FLUXCOM-GSWP3	3	4	4	1	3	2	7	9	5	3
7	FLUXCOM-WFDEI	3	4	4	1	3	2	7	9	5	3
8	MTE	3	4	4	1	3	2	7	9	5	3
9	ERA5-Land	2	4	4	4	4	2	7	12	5	8
10	MERRA-Land	2	4	3	2	4	2	1	12	5	8
11	GLDAS CLSM 2.0	2	4	4	4	4	2	8	2	5	1
12	GLDAS NOAH 2.1	2	4	3	4	4	2	8	8	3	1
13	GLDAS VIC	3	4	3	4	6	2	8	10	5	7
14	CABLE-POP	4	1	4	2	7	1	5	6	1	8

15	CLASSIC	4	1	2	2	7	5	5	6	1	4
16	CLM5.0	3	4	4	4	2	5	9	11	2	6
17	DLEM	4	3	1	3	3	5	8	6	1	5
18	E3SM	2	4	2	2	7	5	5	6	2	5
19	EDv3	4	2	1	5	5	4	6	3	4	7
20	IBIS	2	4	4	1	4	5	2	10	5	7
21	ISBA-CTRIP	4	1	2	2	7	1	5	6	1	8
22	JSBACH	4	2	2	2	7	4	5	12	3	8
23	LPJ-GUESS	4	1	3	2	7	1	5	6	1	4
24	LPJmL	4	1	3	5	3	1	5	6	1	5
25	LPX-Bern	4	1	3	5	7	1	5	6	4	4
26	OCN	2	4	4	1	3	5	8	1	2	3
27	ORCHIDEE	4	1	2	2	7	1	5	6	1	8
28	SDGVM	2	4	1	1	3	5	8	6	5	5
29	VISIT	1	1	2	2	7	3	2	1	1	4
30	YIBs	4	1	2	2	7	5	5	12	1	5

Table S10. The information of 30 ET datasets were trained or validated using FLUXNET observations. The letter “Y” stands for “Yes”, indicating the use of FLUXNET observations; the letter “N” stands for “No”, indicating no FLUXNET observations were used.

ID	Name	Training	Validation
1	PML	Y	Y
2	GLEAM 3.6a	N	N
3	GLASS	Y	N
4	PLSH	N	N
5	FLUXCOM-CRUNCEP_v8	Y	Y
6	FLUXCOM-GSWP3	Y	Y
7	FLUXCOM-WFDEI	Y	Y
8	MTE	Y	Y
9	ERA5-Land	N	N
10	MERRA-Land	N	N
11	GLDAS CLSM 2.0	N	N
12	GLDAS NOAH 2.1	N	N
13	GLDAS VIC	N	N
14	CABLE-POP	N	N
15	CLASSIC	N	N
16	CLM5.0	N	N
17	DLEM	N	N
18	E3SM	N	N
19	EDv3	N	N
20	IBIS	N	N
21	ISBA-CTRIP	N	N
22	JSBACH	N	N
23	LPJ-GUESS	N	N
24	LPJmL	N	N

25	LPX-Bern	N	N
26	OCN	N	N
27	ORCHIDEE	N	N
28	SDGVM	N	N
29	VISIT	N	N
30	YIBs	N	N